2021-06-09

3D Geomechanical Modeling of Shale Formations and its Application in Borehole Stabilization

Deng, Liyu

UNIVERSITY OF CALGARY

3D Geomechanical Modeling of Shale Formations and its Application in Borehole Stabilization

by

Liyu Deng

A THESIS
SUBMITTED TO THE FACULTY OF GRADUATE STUDIES
IN PARTIAL FULFILMENT OF THE REQUIREMENTS FOR THE
DEGREE OF MASTER OF SCIENCE

GRADAUTE PROGRAM IN CHEMICAL ENGINEERING

CALGARY, ALBERTA

JUNE, 2021

Abstract

The issue of borehole instability as seen in shale formation drilling is a major problem currently facing the industry. In recent years, deep exploration and more intensive development of hard and brittle shale gas reservoirs has shown that borehole instability is a widely occurring issue present in this type of strata. Because of the high frequency of catastrophic failures that accompany drilling in shale, this is an important technical problem to be solved. Furthermore, as a result of the recent shale gas revolution in North America, there has been a focus on integrated innovations and the development of multi-disciplinary fields and multiple technologies related to exploitation of this resource.

As part of this ongoing multi-disciplinary approach, the advanced development concept known as geological engineering integration has been put forward. Rooted in the study of geodynamics and aimed at the problem of borehole instability in shale formations, this study explores and develops concepts related to geomechanics, including well location optimization, well trajectory optimization, pre-drilling formation pressure prediction and well wall stability prediction techniques. The meticulous modeling of 3D geomechanics is of great significance to the study of regional borehole stability in a shale formation. Therefore, a geomechanical modeling method for shale formations and its field application in Indonesia's Oilfield A is demonstrated in this thesis. As part of this modeling, a detailed study on the physical, chemical, and mechanical properties of shale in Oilfield A is carried out by laboratory mineral analysis, electron microscopy, cation exchange capacity and rock mechanics

parameters. These experimental results form the cornerstone of the 3D geomechanical modeling of Indonesia's Oilfield A.

Leveraging the Petrel software platform, the 3D geomechanical modeling method and principles of a shale formation are introduced in detail. Through a series of core tests, well logging data and seismic inversion data, the mechanical parameters of Oilfield A are described in depth, and the spatial distributions of important parameters such as 3D elastic modulus, 3D Poisson’s ratio and 3D pore pressure in this oilfield are established. 3D geomechanical models of heterogeneity, porosity and elastoplastic features are also established.

Using the finite element method, the 3D stress distributions and 3D safe density windows of Oilfield A are also calculated. By establishing a 3D fine geomechanical model, various attributes are extracted along the borehole trajectory of well A-10, and a prediction of borehole stability is carried out. The drilling fluid density windows and well depth structure are also recommended, indicating the type and approximate depth of possible downhole complications.

The numerical results of the minimum in-situ stress present in Indonesia's Oilfield A are calibrated by LOT (leaking of test) data. Importantly, the relative errors that exist between LOT data and the minimum in-situ stress are small, and the maximum relative error is only 0.02. The drilling period of well A-10 is 28 days. Compared with the average drilling period of 55 days in Oilfield A, the drilling period is shortened by 49 days as a result of the modeling studied. Importantly, no complex accidents occur in the drilling process.

Through direct or indirect validations of all established 3D pore pressure, collapse pressure, rupture pressure, in situ-stress and other models, both a confident geomechanical model and a density window model are finally determined. The results show that the geomechanical model can accurately reflect the magnitude and heterogeneity of in-situ stress in a shale formation and can effectively solve the problem of regional borehole stability found in this formation.

Acknowledgements

I would like to express the deepest appreciation to my supervisor, Dr. Zhangxing (John) Chen, who provided both support and suggestions for my research and study.

My appreciation also extends to all the members in the BitCan Geosciences & Engineering Inc., and everyone who helped me during my research in University of Calgary.

Finally, I would like to thank my family and all of my friends.

Table of Contents

List of Figures

List of Tables

List of Symbols, Abbreviations and Nomenclature

Symbols	Definition
C	Cohesive strength, MPa
φ	Internal friction angle, radian
σ_1	Maximum principal stress, MPa
σ_3	Minimum principal stress, MPa
P_u	Load during specimen failure, N
D	Diameter of cylinder specimen, m
t	Thickness of cylinder specimen, m
V_p	Compressive wave velocity, m/s
V_s	Transverse wave velocity, m/s
E_d	Dynamic elastic modulus, GPa
μ_d	Dynamic Poisson's ratio
ρ	Density, g/cm^3
E_s	Static elastic modulus, GPa
μ_s	Static Poisson's ratio
PP	Pore pressure, MPa
OBG	Overburden pressure, MPa
PP_N	Hydrostatic column pressure, MPa
DT_N	Normal compacted mudstone acoustic time differences
DT_0	Acoustic delay of mudstone determined by logging
V_N	Velocities of mudstone formation by normal compaction
V_0	Velocities of mudstone formation by logging or earthquake
n	Eaton index
DT_{ml}	Corresponding acoustic time differences
A	Empirical values
B	Empirical values
U	Empirical values
V_{cl}	Mud content of sandstone
S_t	Tensile strength of rock, MPa
ρ_b	Collapse pressure gradient, SG
σ_H	Maximum horizontal in-situ stress, MPa
σ_h	Minimum horizontal in-situ stresses, MPa
α	Biot coefficient
D	Depth, m
ρ_f	Fracture pressure gradient, SG
Q	Tectonic stress coefficient
σ_V	Overburden pressure, MPa
μ	Poisson's ratio

UCS	Compressive strength, MPa
a	Conversion factors
b	Conversion factors
J	Jacobian determinant

Abbreviation

3D	There dimensional
SDK	Software development kit
2D	Two dimensional
LOT	Leaking off test
CEC	Cation exchange capacity
XMAC	Multipole array acoustic logging
DTCO	Longitudinal wave time delay
DTSM	Shear wave time difference
DFIT	Diagnostic fracture injection test
DC	Drilling pressure index corrected by drilling fluid density
DST	Drilling Stem Test

CHAPTER I. Introduction

1.1. Research Background and Significance

Drilling accounts for 50% - 80%[1] of oil and gas exploration and development costs, while the waste caused by borehole instability accounts for as much as 10% - 20%[2] of the total drilling cost. This means that, globally, the annual costs associated with borehole instability are 5% - 16% of the total costs of oil and gas exploration and development. There are numerous reasons for this wastage. Borehole instability affects both a drilling speed and logging and cementing quality. Moreover, it can also make it difficult, if not impossible, to reach a target formation, thereby affecting the outcome of exploration. It is, therefore, crucial to study key technologies that will maintain borehole stability and not only reduce the cost of oilfield exploration and development but also improve economic efficiency.

Sedimentary rocks are the main geological objects of oil and gas drilling, and more than 70% of these sedimentary rocks are shale strata. According to statistics, 90% of borehole instability problems appear in shale strata, in which deep, hard and brittle shale accounts for approximately two-thirds of the issues, and shallow, soft shale accounts for another third[3]. Hard, brittle shale not only has a higher frequency of borehole instability, but the degree of that instability is often more serious. It has been found in an actual drilling process that drilling hard brittle shale formations usually produces a large number of borehole collapse blocks, and leads to frequent

leaks in a drilling fluid and extremely difficult treatment operations. In serious cases, a borehole is scrapped entirely, causing great harm to the overall drilling operation. In southern Argentina, as well as the southern Arabian Gulf, Japan and the Middle East, hard brittle shale is found in deep strata, and downhole there are frequently complex situations which can seriously restrict a drilling process. For example, in southern Argentina's Cretaceous shale formation, natural fractures develop as drilling commences, well walls may collapse during the process, and an expansion rate of some well sections reaches as high as 100%. Because of this serious downhole complexity, the average drilling non-production time exceeds the design time by 75%, greatly increasing overall drilling costs[4].

These types of problems have been encountered in strong tectonic movement zones such as the Junggar Basin, Qaidam Basin, Tarim Basin, Yumen Oilfield, and in the Northeast Sichuan Basin in western China. For example, drilling in the Junggar Basin has involved frequent issues of well leakage, collapse, drilling jam and other complex problems, highlighting an issue where a well diameter expansion rate is often as high as 50%[5]. Similarly, in the Beibu Gulf Basin, the Weizhou 12-1 oilfield's Wei 2 section is made up of hard brittle shale with a thickness around 100-150 m. During directional well drilling in this stratum, borehole collapse is a serious problem as the complexity underground leads to a situation in which well blocking frequently occurs[6].

With rapid developments in the world's economy, the global demand for oil and gas resources has increased greatly, and the crisis of energy supply and demand is

increasing day by day. The development of unconventional energy sources, such as shale gas, has gradually been put on the agenda to alleviate the current energy crisis. Indeed, global shale gas resources are abundant and have broad development prospects. The shortage of oil and gas resources has accelerated the exploration process of shale gas in the world. However, serious accidents involving borehole collapse often occur in hard brittle shale strata, which not only affects effectiveness, but also has an important impact on subsequent cementing quality and fracturing operations. In short, it has become a significant bottleneck restricting shale gas exploration and development[7-11].

In recent years, large-scale development of unconventional oil and gas sources in the United States has met with huge success. As a result, there has been widespread adoption of integrated innovation and development of both multi-disciplinary and multi-technology integrations. This has further established an integrated technical flow in which geological engineering and geomechanics are a key technological link [12-15].

Geomechanics plays an important role in drilling engineering applications such as: pre-drilling engineering preparation; pre-drilling geological design; real-time tracking of positive drilling and optimization of drilling management; support of positive drilling geological guidance tracking; analysis and optimization of complex conditions of drilling; and casing and borehole integrity analysis. Indeed, well location optimization, well trajectory optimization, pre-drilling formation pressure

prediction and well wall stability prediction techniques are all informed by geomechanics.

For the integration of geological engineering, it is necessary to carry out geological modeling, numerical simulation of in-situ stress, and 3D visual display[16] of modeling and simulation results. Among these, crustal stress is the fundamental force that causes shear and tensile failure of borehole rock, and the magnitude of crustal stress directly affects both the collapse and rupture pressure of the surrounding strata. A crustal stress modeling theory[17] was originated at Stanford University in the United States. Its main idea is to accurately find the size and direction of crustal stress (i.e., overburden pressure, minimum horizontal principal stress, and maximum horizontal principal stress), formation pore pressure, and rock mechanical properties (mainly including rock uniaxial compressive strength, an internal friction coefficient, Poisson's ratio, a porous elastic coefficient, and an elastic modulus). On the basis of fine structural modeling, both 3D geomechanical finite element modeling technology and large-scale parallel computing technology are used to complete final calculations. Through the production of a meticulous 3D geomechanical model, various attributes are then extracted along the design borehole trajectory, and the prediction of borehole stability is carried out. In addition, a drilling fluid density window is recommended to indicate the type and approximate depth of potentially complex downhole scenarios. Therefore, 3D stress modeling is of great significance when studying borehole stability in a regional shale formation.

1.2. Introduction of crustal stress

1.2.1. Basic concept of crustal stress

Changes in the rotation speed of the Earth are impacted by celestial bodies. These changes, within and outside the Earth, cause uneven amounts of stress in different parts of the crust. This stress is further affected by extrusion - stretching and twisting, respectively - which promotes the deformation of rock strata in the crust. At the same time, rock formations also produce a force against deformation known as crustal stress. This stress is produced internally and acts on a unit area of the crust. [18-21]. Crustal stress is an objective reality, which is caused by buried depth, lithology, pore pressure, rock structure and a structural model. Because the focus of oil and gas exploration and development is the rock and fluids in a given strata, the crustal stress impacting rock and fluids is the key to studying related engineering problems[22].

1.2.2. Causes of crustal stress

The causes of crustal stress[23-24] are complex. The formation of crustal stress is mainly related to various dynamic processes of the Earth, including: plate boundary compression, mantle thermal convection, Earth's own internal stress, gravity, Earth's rotation, magma immersion and uneven expansion of the crust. In addition, uneven temperature, water pressure gradients, surface erosion or other physical and chemical changes can also cause a corresponding stress field. Among them, tectonic and self-gravity stress fields are the main components of Earth's present stress field. Nowadays, the state of crustal stress is mainly controlled by recent tectonic movement,

but it is also related to historical tectonic movement. For billions of years, the Earth has experienced numerous tectonic movements, large and small, and the stress fields of each tectonic movement have been superimposed, towed and reformed many times. In addition, a stress field is also affected by many other factors, resulting in the complexity and variability of the stress state.

1.2.3. Influencing factors of crustal stress

A distribution of crustal stress found in the deep mass of crustal rock is complex and changeable[25-26]. The root cause of this phenomenon lies in the multi-source and multi-factor influences of crustal stress, but is mainly determined by rock mass weight, geological tectonic movement and denudation. An earth stress field in a given rock mass is a complex stress field within a 3D space. Its size and distribution are affected by many factors, which also brings great influence and uncertainty to the measurement of earth's stress field.

(1) Influence of rock mass weight

The stress present in a rock mass is equal to the weight of the overlying rock mass. The results show that a distribution of crustal stress is basically the same in the deepest part of the earth. However, in the study of initial crustal stress, it is found that the formation factors of stress in a field of rock mass are numerous, and denudation is difficult to reasonably consider. In conventional inversion analysis, only the weight of rock mass and the movement of geological structures are usually considered.

(2) Influence of topography and denudation on crustal stress

The influence of topography and geomorphology on crustal stress is complex, and denudation also has significant influence on crustal stress. Before denudation occurs, there is a certain amount of vertical stress and horizontal stress present in the rock mass. After denudation, the vertical stress decreases, but much of the stress has no time to release and still retains the original amount of stress. However, the horizontal stress is minimally released and is basically retained as the original stress quantity, which leads to the existence of a much larger stress value in the rock mass than the deadweight stress caused by the existing formation's thickness.

(3) Influence of tectonic movement on crustal stress

From the point of view of energy, crustal stress is actually a process of energy accumulation and release. Because the magnitude of crustal stress in rock is limited by the rock's strength, it can be said that in the same geological structure, the magnitude of crustal stress is a function of lithologic factors. Rock masses with great elastic strength are beneficial to the accumulation of crustal stress, so earthquakes and rock bursts occur easily in these parts, while plastic rock mass is not conducive to the accumulation of stress because of its easy deformation.

(5) Influence of water and temperature on crustal stress

Groundwater has a significant influence on the scale of crustal stress present in a given rock mass. The rock mass contains joints, fissures and other disconnected layers. These fissures often contain water, and the existence of this groundwater causes water pressure to build up within rock pores. This pressure, along with the stress present in the rock skeleton, constitutes the crustal stress of the overall rock mass. Temperature

also has an important influence on crustal stress, and this is mainly reflected in a geothermal gradient and the local temperature of a rock mass. Because of the geothermal stress caused by geothermal gradients, the temperature stress field of a rock mass is a static pressure field, which can be algebraically superimposed with the weight of the stress field. If the local conditions of cold and heat in a rock mass are uneven, it will produce shrinkage and expansion. This then causes the rock mass to produce crustal stress.

1.2.4. Distribution of crustal stress

(1) Crustal stress is a stress field with relative stability and is a function of time and space.

The magnitude and direction of the three principal stresses vary with space and time, thus creating a non-uniform stress field[27-28]. A spatial variation of crustal stress is obvious from a small scale, but for a region as a whole, it is not. For example, in Northern China, the main compressive stress from east to west is near the northwest. In some areas where earthquakes are active, the magnitude and direction of crustal stress change with time, which is also very obvious. Before an earthquake occurs, there is a stage of stress accumulation in which a stress value increases continuously. When an earthquake strikes, the concentrated stress is released, and there is both a sudden and large decrease in the overall stress value. The direction of principal stress will change greatly when the earthquake occurs, and then return to its initial state for a period of time.

(2) The measured vertical stress is basically equal to the weight of the overlying strata.

Hoek and Brown[29] summarized a pattern of measured vertical stress with a depth of *H*. According to their findings, the measured vertical stress increases linearly within a range of 2500-2700m. If the buried depth is less than 1000 m, the measured value may be very different from the predicted value, some of which may be five times different. Therefore, this equation can be used to estimate the mean value of all stress measurements, but it must not be used to obtain the exact value at any particular position.

(3) The maximum horizontal principal stress and the minimum horizontal principal stress also increase linearly with depth.

The maximum horizontal principal stress and the minimum horizontal principal stress generally differ greatly, showing strong directionality. The above distribution pattern of crustal stress will also be affected by topography, surface erosion, weathering, rock mass structure characteristics, rock mass mechanical properties, temperature, groundwater and other factors, especially the disturbance of topography and faults.

1.3. Study on measurement method of crustal stress value and direction

The crustal stress present in a given rock mass is the most basic and important engineering load when it comes to rock mass engineering. It is one of the initial conditions necessary for numerical calculations of engineering issues in a rock mass

and the basic factor for analyzing the failure and displacement characteristics of a rock mass. In general, the direction and approximate stress values of earth's modern stress field can be obtained through geology, seismology and surveying methods. These direct measurement methods[30] include hydraulic fracturing and the Kaiser effect of acoustic emission. The regional geological background and various influencing factors should be analyzed to determine the reliability of a measured value; otherwise, the quality of the measured value will be greatly reduced. Understanding the influence of factors related to crustal stress measurements and the importance of reliability in the analysis exceeds a measurement itself to some extent. An uncertain measurement value is meaningless and can even become misleading.

1.3.1. The Kaiser effect of acoustic emission in the measurement of crustal stress

Compared with both traditional stress relief and hydraulic fracturing methods, the Kaiser effect of rock acoustic emission has the advantages of fast speed, low cost and fewer limitations, which is convenient for a large number of tests that seek a regional law of a crustal stress change. Therefore, this method is a promising one for measuring crustal stress. However, despite these advantages, there are still many problems in a measurement of crustal stress using the Kaiser effect, among which the most important problem is how to determine the direction of crustal stress. Before, engineers used the Kaiser effect to measure original rock stress by a range of 180°. This meant that they needed more samples and testing workloads, which has high cost. At the same time, due to the action of multi-period tectonic movements, the structure

of a rock mass can change, and the magnitude and direction of tectonic stress or original rock stress in a region can be seen to have changed quantitatively and qualitatively. In the past, however, the Kaiser effects were measured in the horizontal or vertical direction, so it was possible that none of the samples were in the direction of the principal stress. The results of these tests were a partial force of the earth stress field, which is different from the true original rock stress value, and even further away. Because of these reasons, the application of the Kaiser effect in measuring the original rock stress cannot, in practice, be brought into full play. Presently, there are attempts to push the acoustic emission technology to a new practical stage. The main results are as follows: through field directional coring technology, 3D stress, i.e., the magnitude and direction of the three principal stresses, is measured indoor, and the accuracy of the principal stress values is further improved. The Kaiser effect then measures the crustal stress of a rock mass based on the acoustic emission effect of the rock's material. But in fact, only the maximum stress value of the historical rock mass is measured, which means that it can only be used as an auxiliary means of a borehole stress measurement.

1.3.2. Measurement of crustal stress by hydraulic fracturing

Hydraulic fracturing uses two expandable rubber packers several meters apart to seal a section of a borehole at a known depth. The borehole is then pressurized by a pumping fluid, and a relationship curve of fluid pressure with time is recorded. The theoretical basis of this method is to assume that the rock mass is linearly elastic,

isotropic and impermeable, and that one principal stress direction of the rock mass is parallel to the borehole axis. Therefore, a recording curve can be analyzed and calculated, the magnitude of the two principal stress values in the plane perpendicular to the borehole axis can be obtained, and the azimuth of the two principal stresses can be seen by the azimuth of a crack. When the borehole is vertical, the principal stress along the borehole axis is calculated according to the weight of the overlying strata.

Hydraulic fracturing is one of the most effective and widely used methods for crustal stress measurement. This method can directly measure crustal stress, and its results are in a large range of average stress. It can also be measured in wells at depths of thousands of meters and helps in obtaining complementary data alongside acoustic emission. Compared with other methods, hydraulic fracturing has a big defect; that is, the direction of principal stress is not very accurate. However, it has the advantages of simple equipment, convenient operation, continuous or repeated testing at any depth, fast measuring speed, an intuitive measuring value and a large representative value. Therefore, this method has been paid more and more attention and popularized, leading to its global application as an advanced method for directly measuring deep hole stress.

1.3.3. Determination of direction of crustal stress by borehole collapse

Since the 1970s, many scholars have found that rock caving often occurs in deep drilling, and the long axis direction of an elliptical cross section is often the same at different depths of the same drilling. In underground roadways, this caving

phenomenon is also found. The long axis direction of an caving ellipse is parallel to the minimum horizontal principal stress direction. According to this phenomenon, a drilling collapse method has been developed for determining crustal stress. As shown in Figure 1.1, the long axis direction of the shaft wall caving ellipse is always consistent with the direction of the minimum horizontal main crustal stress. That is, perpendicular to the direction of the maximum horizontal crustal stress, the direction of crustal stress can be determined by using the shaft wall caving ellipse. At present, the most commonly used instruments for measuring a borehole ellipse are: ultrasonic downhole measuring instruments and a four-arm formation inclination logging instrument.

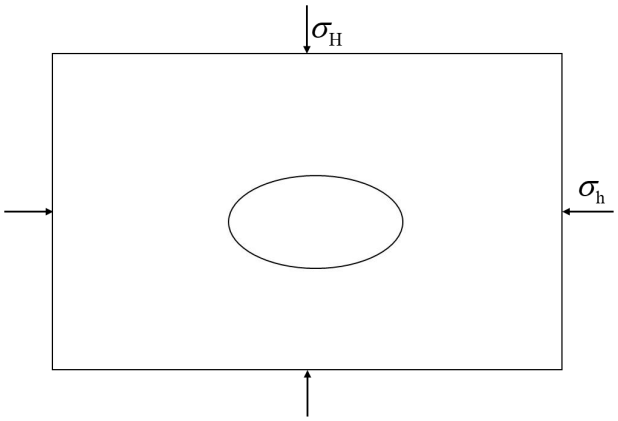

Fig. 1.1. Borehole caving ellipse

1.4. Study on 3D calculations of crustal stress

In the process of oil and gas field exploration and development, it is difficult to carry out crustal stress field monitoring for a whole oil and gas field area, which, in turn, significantly increases development costs. In order to extend from limited stress measurements to a regional range, structural stress field analysis and numerical

simulation calculations are needed. The traditional 3D crustal stress modeling method is to calculate the crustal stress data of a single well based on logging data and seismic data, and then use interpolation algorithms to form the whole oilfield stress field. Importantly, this method cannot reflect the influence of formation heterogeneity and a dip angle on a distribution of crustal stress [31]. Hashimoto et al. (2006), Zeng et al. (2013), Jiu et al. (2013), Guo et al. (2016) and Liu et al. (2017) successfully simulated 3D stress fields of their study areas using a methodology known as the finite element stress analysis method[32-36]. However, a single finite element analysis software package cannot establish a detailed 3D geological model which reflects reservoir heterogeneity. To address this deficiency, Liu et al. (2016) developed a series of algorithms to realize the bidirectional conversion of both the Petrel software platform and ANSYS software platform. Firstly, they used Petrel to establish a 3D heterogeneous geological model for a target area, and then imported the 3D geological model into the ANSYS software platform. Finally, they simulated 3D ground stress in the target area using the finite element method[37]. At present, the mainstream geological modeling software such as Petrel and Jewel Suite has developed to a more mature state. In addition to completing traditional 3D geological modeling, a meticulous 3D geomechanical model for a research area can be achieved by filling in a new geomechanical module.

Petrel[38] is a large integrated software platform developed by Schlumberger, and it is also a platform for the integrated work of reservoir exploration, development, and post-processing. It achieves the integration of reservoir engineering, which includes

phase modeling, physical attribute modeling, data processing analysis, and mesh simplification. Petrel takes a geological model as the center, and then runs through the whole process from seismic interpretation to reservoir numerical simulation and to oil and gas exploitation. Against the background of more and more complex oil and gas reservoir development environments, Petrel has established an open and shared environment that allows geological, seismic, logging, reservoir, drilling, and data management in order to share knowledge and achievements across many fields. This platform now has a leading position in the field of oil exploration and development.

Petrel's modeling uses a combination of structural modeling and multi-point modeling and, more importantly, a model also features automatic updating. On the display, it uses 3D visualization technology to put forward interpretations of stratigraphic information. In the treatment of formation fractures, it uses fracture system analysis technology and fracture system automatic extraction technology. Petrel not only has a beautiful interface, and it is also easy to operate and contains complete and more advanced functions than other similar tools. This advanced technology, convenient interface, complete development process, convenient data processing method, appealing graphic display, and the fusion of knowledge across various disciplines and specialties allow users across many disciplines to interact freely, and have created a very monopolistic technical advantage.

Among these many advantages, a geomechanical model can quickly generate a high-quality hexahedral finite element mesh, endow each finite element node with different material parameters, fully consider the influence of faults and natural cracks

on crustal stress, and describe the heterogeneity of the whole research area perfectly. 3D stress in this model is calculated using the finite element method. Geomechanical modeling can also directly inherit the results of other geological models, including stratigraphic occurrence, fault development and fracture zone distribution, so that the results of geomechanical calculations reflect the characteristics of under-crustal stress more truthfully.

At the same time, single well rock mechanical parameters calculated by logging, core and test data can be directly used to establish the unit properties around a borehole, and may also be used for quality control of a 3D geomechanical model. Indeed, seismic data and information about a geological structure are used to interpolate between wells to ensure the reliability of geomechanical parameters in a 3D space. From a geomechanics module to modeling, and calculations to results analysis, all operations can be completed using the Petrel platform. The models and results can be controlled and displayed in a 3D window. Petrel provides rich and convenient 3D attribute display functions, including along the IJK unit number display, along any section display, joint well section display, and interpretation window display.

In addition, the Jewel Suite platform[39] by Baker Hughes is a software program which integrates regional analysis, reservoir analysis and engineering applications. The Jewel Suite subsurface modeling software has the function of formation contrast structure modeling, which realizes 3D spatial joint well profiles, small formation adjustments, and construction models. It has 2D/3D data displays and interpretations,

2D/3D level automatic tracking, interpretations of results quality control, attribute extraction, information interpretations and other functions. It can also realize the goal-based modeling method and sequential Gaussian modeling method, and can carry out well location design and optimization functions including 3D spatial well location design, trajectory optimization and precision assurance. This technology also includes data preprocessing, capacity prediction, residual oil research, fracture diversion capacity evaluation and capacity prediction ability. The Jewel Suite GeoMechanics module can make use of structural models. It uses data from 1D crustal stress models to establish a model with complex geological conditions. It also takes into account the influence of faults and quickly establishes a 3D static crustal stress model combined with seismic attributes. The Jewel Suite reservoir modeling software can also be combined with the Dassault Systems powerful finite element mechanical simulator and Abaqus finite element analysis software. The Abaqus software simulates nonlinear stress, large deformation, compaction and settlement of oil and gas reservoirs in production by proved algorithms. The synthetic Jewel Suite 3D geomechanical software system enables users to quickly establish efficient digital simulations to support parameter studies and help determine uncertainties in reservoir development models. A larger full-field 3D reservoir view is condensed into an easily manageable, high-resolution geomechanical simulation map.

Beijing Wanggetiandi Software Technology Corporation has a set of comparative modeling SDK (Software Development Kit) software, which has an algorithm library[40] suitable for complex geological structure modeling. The core of the

algorithm is to use triangulation and optimization techniques. These techniques enable users to generate ideal and fine 3D models based on original data, and then automatically judge faults and relationships between strata. In addition, geologists often have different views and opinions, so the software also takes into account the understanding of geologists in the modeling process. In this way, it more accurately describes the actual situation of strata.

The company also has a crustal stress simulation calculation module. Its principal use is the numerical simulation method to calculate the magnitude and direction of crustal stress and its spatial distribution state in a certain period. This module can also predict the direction of artificial fractures and analyze the stability of artificial fractures. The main functions include: calculating the petrophysical property parameters including density, Young's modulus, Poisson's ratio, friction coefficients, tensile strength and shear strength. It also has the option to perform numerical interpolatiosn and model a 3D display. The module can show the setting of complex mechanical boundary conditions, including a normal phase constraint and an arbitrary direction constraint. 2D and 3D displays are optional and include the calculation results. Finally, it is useful for outputting high-resolution documents.

Hengtaiaipujituan Corporation also makes comprehensive use of geological, drilling, and seismic data as well as other data based on the development of geological modeling. The difference is that this company uses a fast corner grid partition algorithm, plus 3D visualization technology. These techniques make the computation and presentation of massive grids a reality.

The GeoTalk software developed by Hengtai Aipu Company[41] can use geological, drilling and logging data to establish geological models and mechanical models, and use 3D finite difference numerical simulation methods to simulate the crustal stress in a study area. However, the software uses a curved sheet as a mechanical model used in reservoir structure simulation, which cannot truly reflect the structural changes of strata.

1.5. The main research objectives and methods

The main contents of this thesis are as follows:

(1) Experimental study on physical, chemical and mechanical characteristics of a shale stratum, including mineral analysis, electron microscope scanning, cation exchange capacity and the mechanical parameters of shale in the study area.

(2) 3D geomechanical modeling of the shale stratum.

Using the Petrel software platform, Indonesia's Oilfield A is selected. Through a series of core tests, well logging data and seismic inversion data, the mechanical parameters of the shale formation present in Oilfield A are described in detail, and a spatial distribution of important parameters such as a 3D elastic modulus, a 3D Poisson ratio and 3D pore pressure are established. By using the finite element numerical simulation method, a 3D stress distribution and a 3D safe density window for Indonesia's Oilfield A are also calculated.

(3) Providing comprehensive analysis and technical countermeasures for well A-10 in Indonesia's Oilfield A.

Drilling engineering preparation before drilling: Based on a meticulously calculated 3D geomechanical model, a prediction of borehole stability is carried out along a design borehole trajectory. Furthermore, the drilling fluid density window and casing design are optimized, the potential drilling complex conditions (leakage and drilling jam) are analyzed, and warnings are made regarding risky well sections.

Real-time tracking and drilling management optimization: Using the latest drilling data, the 3D geomechanical model for a single well and two platforms is updated, the model's accuracy and prediction accuracy are improved dynamically, and the drilling fluid density window is adjusted and optimized in time. Combined with real-time drilling parameters and logging data, complex events in the drilling process are analyzed, and the corresponding optimization measures are put forward to improve drilling time and reduce risk.

(4) Model calibration.

LOT (leaking of test) data from Oilfield A, including complex conditions during drilling, drilling and completion data, and well A-10's data, is used to validate the established geomechanical model and safety the density window model.

CHAPTER II. Physical and Chemical Characteristics and Mechanical Characteristics of Shale Rock

Because of the widespread occurrence and high frequency of catastrophic issues related to borehole instability, hard brittle shale[42] has become the focus of borehole stability research. In recent years, due to deep exploration and development of shale gas resources, borehole instability found in this kind of strata has become an important technical problem to be solved. When drilling hard brittle shale in a field, serious borehole collapse often occurs, resulting in a large amount of hard shale debris that may result in drilling blockages, the burial of drilling tools or complete borehole abandonment, all of which lead to huge economic losses. In conclusion, the existence of these problems is mainly due to the lack of in-depth understanding of mechanisms related to borehole instability and the influencing factors of shale. In order to study the mechanisms in shale that lead to borehole instability, the mechanical characteristics of hard brittle shale must be studied, and the physical and chemical properties of hard brittle shale must be fully understood.

The study of shale's physical and chemical properties is the basis for the study of borehole stability. Mud shale contains a large amount of hydrated clay minerals, which can react with water. The water absorption process and reaction process of shale are very complex, so the mechanism must be studied and expounded from the microscopic point of view. At the same time, shale has a complex internal structure, showing strong anisotropy, and most shale shows low porosity and low permeability. The above characteristics of shale determine the complex physical and chemical

reactions between shale and a drilling fluid. The material energy exchange and transfer between shale and the drilling fluid is a coupling process. The physical properties and structural characteristics of shale determine a water absorption process of shale. Water absorption can lead to changes in shale's physical properties and structure at any time. Therefore, only by fully studying the material composition, structural characteristics and mechanical properties of shale can the stability of shale boreholes be studied accurately and effectively.

2.1. Classification of clay minerals and shale

Clay shale is composed of clay mineral[43] and other minerals, but the main cause of shale's complex hydration is the abundance of clay minerals contained within. Because clay minerals can be transformed, the properties of shale vary greatly. Mud shale is a clastic sedimentary rock composed of non-clay minerals, crystalline clay minerals and amorphous clay minerals. Among them, non-clay minerals mainly include quartz, feldspar, calcite, and dolomite. The crystalline clay minerals mainly include montmorillonite, illite, chlorite, kaolinite, montmorillonite-illite mixed layer, and chlorite-montmorillonite mixed layer. In summary, the main component affecting shale stability is clay minerals.

2.1.1. Clay mineral

Clay minerals belong to silicate minerals, which are composed of silica tetrahedra and aluminum-oxygen octahedra. These crystals form the basic minerals of clay - montmorillonite, illite, kaolinite and chlorite, through different 2D

arrangements. Among them, montmorillonite has the strongest hydration property, while kaolinite has stable physical properties.

Kaolinite's crystal layer is adjacent to or stacked between O and OH or layers of the kaolinite structure. The main connection force is a hydrogen bond between hydroxyl and oxygen atoms, which closely connects an adjacent crystal layer and prevents the entry of water molecules. There is almost no cation exchange on a surface. On the other hand, interlayers of montmorillonite structures are O and O, and the connection force between these crystal layers is mainly the van der Waals force. In this structure, the interlayer connection is very weak, and water molecules and exchangeable cations can easily enter a crystal layer. Therefore, its cation exchange capacity is very large, about 70 - 130mg/100g dry soil.

Illite and montmorillonite are the same 2:1 structural units, but potassium ions are embedded in a hexagonal structure between silica tetrahedron layers to form strong bonds and prevent water molecules from entering the crystal layers. The cation exchange capacity of illite is also lower than that of montmorillonite, which is 10-40mg/100g dry soil. The structure of chlorite is similar to that of illite. Compared with illite, there is one extra brucite octahedron in two silica tetrahedra. Since the Mg^{2+} displacing Al^{3+} counteracts the positive charge loss caused by the Al^{3+} displacing Si^{4+}, the chlorite interlayers are mainly hydrogen bonds formed on an octahedron of magnesium hydroxide, so chlorite generally does not have expansibility. The structures of kaolinite, montmorillonite and illite are shown in Figure 2.1.

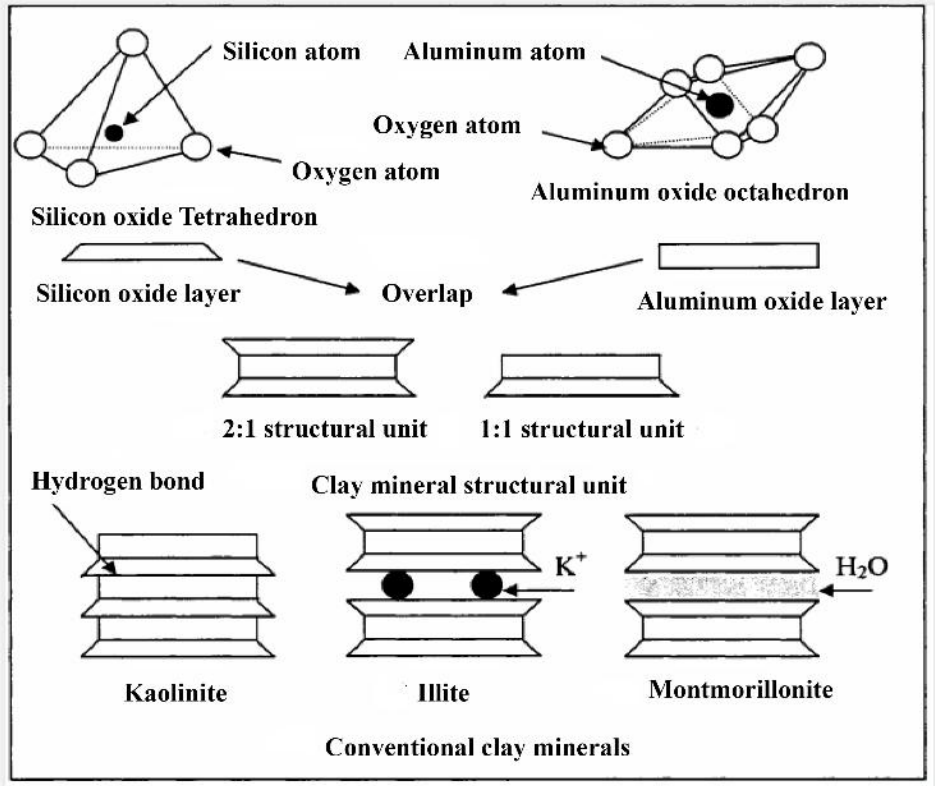

Fig. 2.1 Clay mineral micorstructure diagrams

The morphologies of montmorillonite, illite, kaolinite and chlorite in a microscopic state are different (Figure 2.2). Montmorillonite is flaky, connected in a honeycomb pattern, and its pore edge shape is that of a lotus leaf or petal. Illite, on the other hand, is leaf-like and silky and is attached to a surface of particles or filled in intergranular pores. Microcrystals, such as flakes, divide pores into many small pores, increasing the degree of detour. Filaments are easily washed away by water, blocking both pores and throats and reducing both porosity and permeability. Contrastingly, kaolinite is shaped much like a book-page. It is worm-like or accordion-like, and mostly exists in intergranular pores in the form of pore filling. Its intergranular structure is relatively loose, and easily moves with a fluid under the scour of the fluid, thus blocking and dividing pores, and roars, especially in small roars. This makes

kaolinite very influential and it is an important quick-sensitive mineral. Finally, chlorite possesses a hairy globular shape. It is rose-like and pointed leaf-like, making it so the acicular chlorite is generally attached to a surface of pore particles, and the rose-like, hairy globular chlorites are generally present in pores as fillers. The content of iron ion in authigenic chlorite is rich and has strong acid sensitivity.

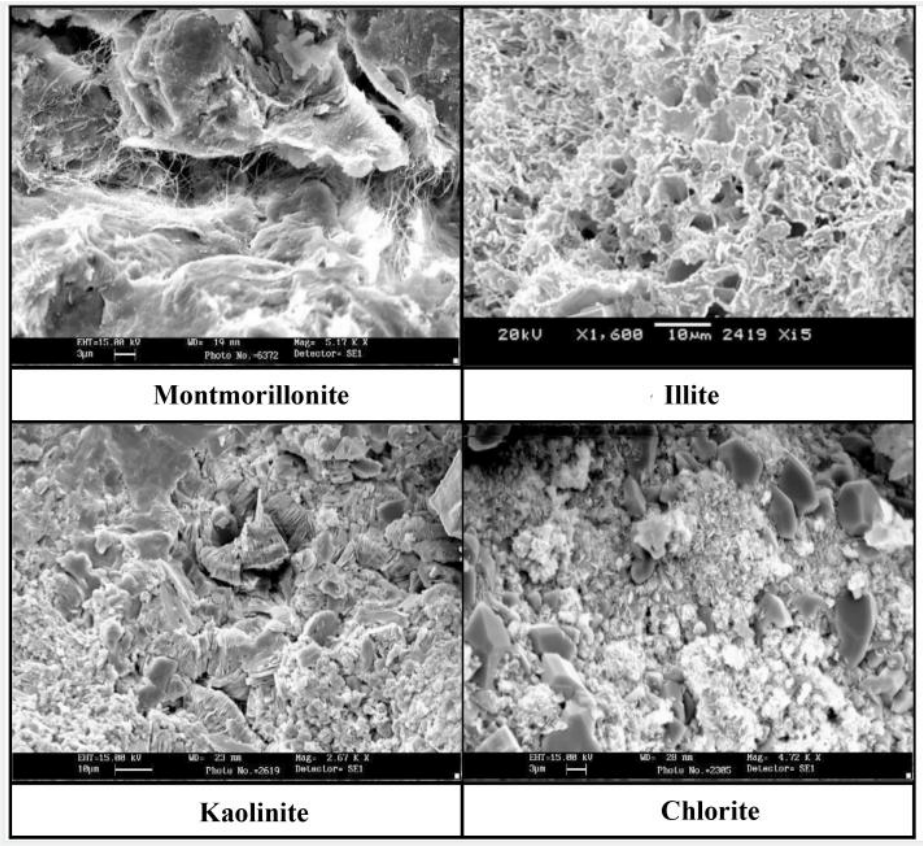

Fig. 2.2. Microstructure photos of common clay minerals

2.1.2. Classification of shale rocks

Mud shale is the most common formation mineral found during drilling, and at least 75% of sedimentary basins are mud shale. Mud shale contains clay, quartz, feldspar, mica, pyrite, organic matter and other minerals, among which the clay and quartz content is high. The microstructure characteristics of shale are shown in Figure

2.3.

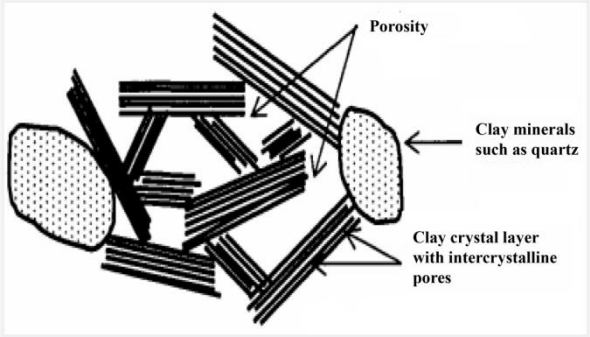

Fig. 2.3. Microstructure diagram of shale

The content of clay minerals in mud shale is determined by a sedimentary environment and sedimentary history. In the process of mud shale diagenesis, clay minerals are transformed through complex physical and chemical processes, which leads to changes in mud shale properties. The mud shale then can be seen as a transition mineral from mudstone to shale, which has the hydration property of mudstone and the hard brittle property of shale. The mud shale properties mainly formed by compaction are closer to mudstone, and the cementation between mineral particles is less. This means that it is easy to destroy when exposed to an natural environment or water, leading to a decrease in overall strength. Mud shale, with its strong compaction and cementation, is closer to shale, which has high strength and weak hydration. The physicochemical properties and relative mineral contents of these two types of mud shale are shown in Table 2.1[44].

Table 2.1 The classification and physical property parameters of shale

Broad heading	Subdivision	Main physical and chemical properties			
		Clay mineral content	Expansivity (%)	CEC (mmol/100g dry soil)	Recovery rate (%)
Soft Mud shale	High expansion Disperse mud shale	Large S, some I	>30	>22	<20
	Easy to expand Easily dispersed mud shale	Rich S, large I, some C	5~30	10~22	20~30
Hard brittle Mud shale	Middle Inflation Middle dispersed mud shale	Large S/I and I, some C	14~20	2~18	30~60
	Not easy to expand Expansion and dispersion mud shale	Medium I, large I/S, some C	7~14	3~12	60~90
	Low expansion Weakly dispersed mud shale	Large I, medium K and C	<5	1~8	>90

It can be seen that the classification essence of mud shale reflects the diagenetic process of mud shale. The more mature the mud shale is, the greater the change of its properties than the initial state. According to the process of mineral diagenesis, mud shale can also be divided into six categories[45]:

(1) Mud shale contains a large amount of montmorillonite, which means there is minimal hardness, with both high expansion and dispersion;

(2) Most of the montmorillonite in mud shale has been converted into an illite-montmorillonite mineral mixture or simply illite. In this case, the hardness is increased, and the expansibility and dispersion are decreased;

(3) Collapsed hard mud shale, which does not contain pure montmorillonite, has been transformed into illite or an illite-montmorillonite mineral mixture. There may

be micro fractures in the shale;

(4) Collapsible hard mud shale, in which the clay mineral content in the shale is about 20-40%, while the rest is quartz and feldspar. Most of the clay minerals are illite and chlorite and, therefore, have poor expansion and dispersion;

(5) Very hard, brittle mud shale, which has micro-fractures in its interior. After a fluid invades the fractures, the strength of a fracture surface decreases and the fractures along the fracture surface occurs;

(6) Crushing mud shale, which has internal cracks and good connectivity. Water molecules easily enter these cracks, resulting in mud shale damage.

The first and second types of mud shale have strong homogeneity, easy hydration and expansion, which leads to a decrease in its own strength. Compared with the first two types of mud shale, the third to fifth types of mud shale have higher strength and a lower degree of hydration and softening. Influenced by diagenesis, micro-fractures develop internally, which form channels through which water seeps into the inner mud shale. The formation of the sixth type of mud shale requires strong tectonic movement, and the distribution of this type is not universal. Affected by the conditions required for mineral transformation[46-47], the third - fifth types of mud shale are generally buried deep and are brittle. Boreholes are prone to collapse under the combined action of mechanics and chemistry where these types are present. It is one of the most common but complex lithologies found in a drilling process. Furthermore, the third - fifth types of mud shale contain hydrated mineral montmorillonite (in an illite-montmorillonite mixture) and a large number of

microcracks develop internally. In order to maintain the stability of a mud shale borehole, we must consider these characteristics of mud shale and make corresponding measures.

2.2. Clay mineral composition

Different clay minerals have different physical and chemical properties. The relative content of clay minerals determines the physical and chemical properties of mud shale. The order of water absorption and expansion of each clay mineral is as follows: montmorillonite > illite > kaolinite > chlorite. Therefore, to understand the physical and chemical characteristics of hard brittle mud shale, it is necessary to determine the relative content of various clay minerals found in hard brittle shale.

2.2.1. X ray diffraction technology

The most widely used method to determine shale mineral composition is X ray diffraction technology[48]. The principle underlying this technique is that each material component has its own characteristic diffraction pattern, and the diffraction intensity is proportional to its content (not strictly established). In a mixture, the diffraction pattern of each material component is independent of the existence of other material components. That is, the diffraction pattern of a sample is composed of the diffraction patterns of each component substance in the sample. This is the basis for quantitative analysis of X ray diffraction. When testing, samples with a particle size of less than 10μm and less than 2μm should be extracted by a water suspension separation method or centrifugal separation according to the Stokes settlement theorem in hydrostatics. A

sample with a particle size of less than 10μm is used to determine the total relative content of clay minerals in the original rock. Clay mineral samples with a particle size of less than 2μm are used to determine the relative content of each clay mineral in the total amount of clay minerals. Figure 2.4 is a physical diagram of polycrystalline X ray diffractometer.

Fig. 2.4 The diagram of polycrystalline X ray diffraction instrument

2.2.2. Experimental results of mineral composition

In this thesis, mud shale drilling samples (Figure 2.5) from well A-1 in Indonesia's Oilfield A were analyzed and the relative content of clay minerals present in the samples was determined by polycrystalline x-ray diffractometer (Figure 2.4). The experimental samples contain mud shale from the Cisubuh, Parigi, and Cibulakan Atas formations.

The rock analysis results from the shale x-ray diffraction are shown in Tables 2.2

and 2.3. As seen, the Cisubuh formation has the highest clay mineral content, up to 30.6%, followed by the Parigi formation at 22.3%. Finally, the Cibulakan Atas formation was the lowest at 15.3%. In general, the clay content present in these three formations is not high, but all of them contain montmorillonite, which means that the formations all possess strong water absorption expansion. The content of montmorillonite in the Parigi formation was the highest - up to 8.0% - followed by the Cisubuh formation at 6.6%, and finally the Cibulakan Atas formation at 4.2%. In terms of actual drilling, the Cisubuh formation represents a serious section of borehole instability. Large quantities of hard mudstone debris are produced as a result of collapse during a drilling process.

Fig. 2.5 Some shale drilling debris samples from well A-1 of Indonesia Oilfield A

Table 2.2 XRD test of Indonesia Oilfield A well A-1

Formation	Depth, m	Clay Mineral, %				Total Mineral Clay %
		kaolinite%	Illite %	Smectite %	Chlorite %	
Cisubuh	450-455	9.19	4.88	10.73	4.19	29
	510-515	7.55	8.16	3.81	1.62	21.1
	570-575	5.8	7.21	11.01	3.54	27.6
	630-635	9.64	4.42	7.98	6.14	28.2
	690-695	8.75	7.62	9.2	3.39	29
	750-755	7.19	7	9.66	4.83	28.7
	810-815	7.8	8.41	6.88	7.48	30.6
	930-935	0.8	0.78	1.31	0.83	3.7
	990-995	7.61	2.58	6.6	6.05	22.8
	1050-1055	1.95	0.89	2.31	1.51	6.7
	1110-1115	2.29	2.52	4.98	3.16	13
	1150-1155	4.71	2.98	4.9	3.71	16.3
Parigi	1270-1275	4.2	4.18	6.46	2.75	17.6
	1330-1335	2.91	3.05	4.98	2.96	13.9
	1390-1395	4.59	4.04	9.95	5.7	24.3
	1430-1435	8.43	4.42	10.65	8.2	31.7
Cibulakan Atas	1550-1555	3.92	3.67	4.75	3.09	15.4
	1610-1615	8.21	3.31	7.08	6.21	24.8
	1660-1665	7.19	3.47	3.1	2.49	16.2
	1710-1715	3.88	3.7	4.81	2.94	15.3
	1810-1815	3.71	3.63	4.4	2.74	14.5
	1970-1975	3.87	3.24	4.04	3.12	14.3
	2030-2035	4.77	5.64	3.42	1.02	14.9
	2090-2095	8.82	6.6	5.19	3.12	23.7

	2150-2155	11.26	3.1	1.05	1.05	16.4

Table 2.3 Mean clay mineral content of cuttings from Indonesia Oilfield A well A-1 well

Formation	Depth m	Total Clay %	Kaolinite %		Illite %		Smectite %	
		Average	Average	Trend	Average	Trend	Average	Trend
Cisubuh	450-1225	22.9%	6.1%		4.8		6.6	
Parigi	1230-1455	22.3%	5.0%		3.9		8.0	
Cibulakan Atas	1470-2155	15.3%	6.2%		4.0		4.2	

2.3. Characteristics of clay mineral structure

In analyzing the borehole stability of mud shale, it is apparent that the cracks present in the rock are not the cause of instability, but rather they induce some physical or mechanical processes and physicochemical processes on s surface of a borehole, which ultimately reduces the resistance of the rock. Therefore, in order to study borehole instability found in hard brittle mud shale, it is necessary to analyze the mud shale's internal microstructure.

The historical and geological factors of fracture formation in rock mainly include the gravity settlement and compaction process, physical and chemical reactions, and finally water loss caused by a pressure increase. The composition, structure, state and properties of mudstone are mainly determined by the stages and conditions of its diagenesis process, while gravity subsidence and geochemical processes play a vital role in diagenesis. The physical and chemical reactions of sediments in diagenesis are gradually replaced by gravity compaction. Then, the granules of mud shale are

gradually transformed into flake structures and further align to form a certain directional sedimentary body. Moreover, due to a further increase in the particle contact number and area, mud shale begins to consolidate and harden[49]. In addition to high temperature and pressure in deep strata, mud shale dehydration, a decrease in water content, an increase in brittleness, and both shrinkage and structural extrusion result in the development of microcracks in hard brittle mud shale.

Generally, a microstructure in mud shale is analyzed by electron microscope scanning, and the width, density, roughness and filling[50] of a fracture surface can be determined by electron microscope scanning. For the purpose of studying the crack opening degree in hard brittle mud shale, this thesis has carried on electron microscope scanning experiments for the hard brittle mud shale obtained from Oilfield A. Four groups of rock blocks are numbered as rock samples 1-4, respectively, as shown in Figures 2.6 to 2.7. According to the analysis results, the samples are compact, but there is a hole seam between the grains, and the width of the hole seam is about 5-10 μm. Some samples are filled with calcite between mud. Where illite-montmorillonite is mixed, layers or flakes appear, and the planal structure and intergranular pore joints are conducive to drilling fluid seepage. All of these circumstances ultimately have adverse effects on borehole stability.

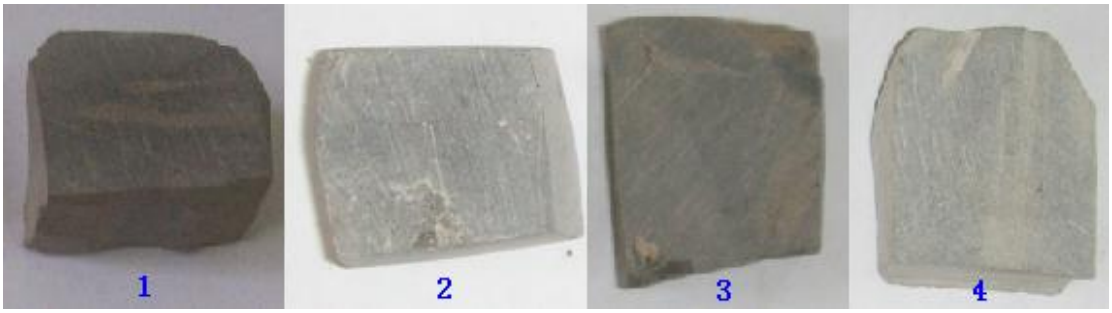

Fig. 2.6 Hard brittle shale blocks of Indonesia Oilfield A

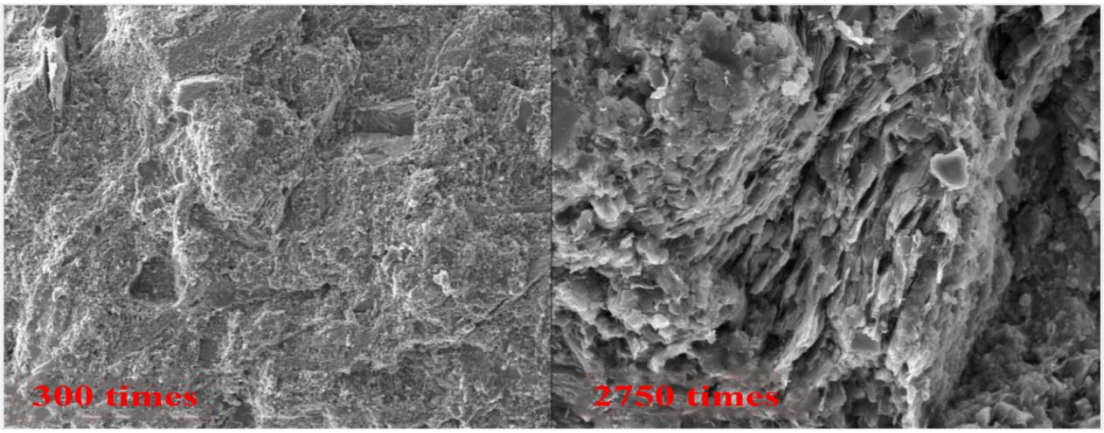

Fig. 2.7(a) Scanning electron microscopic image of the shale sample numbered 1

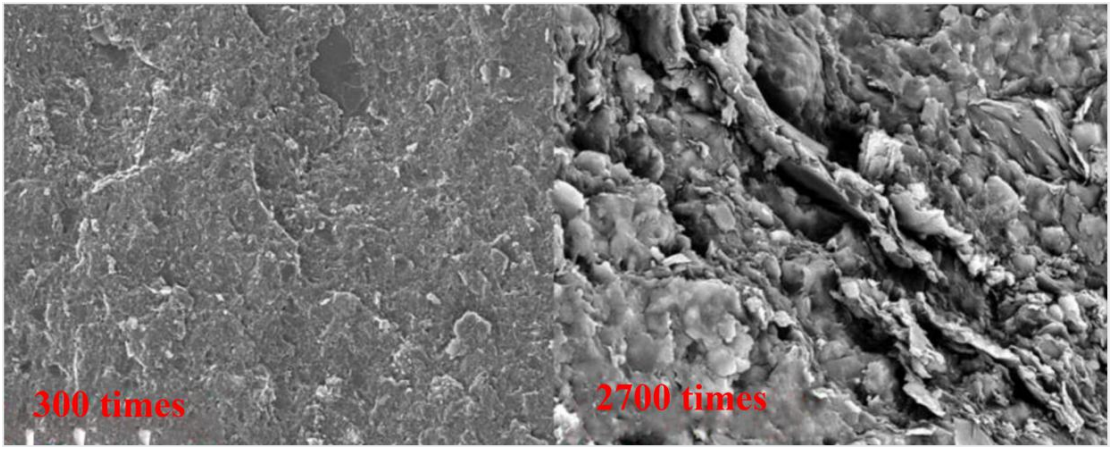

Fig. 2.7(b) Scanning electron microscopic image of the shale sample numbered 2

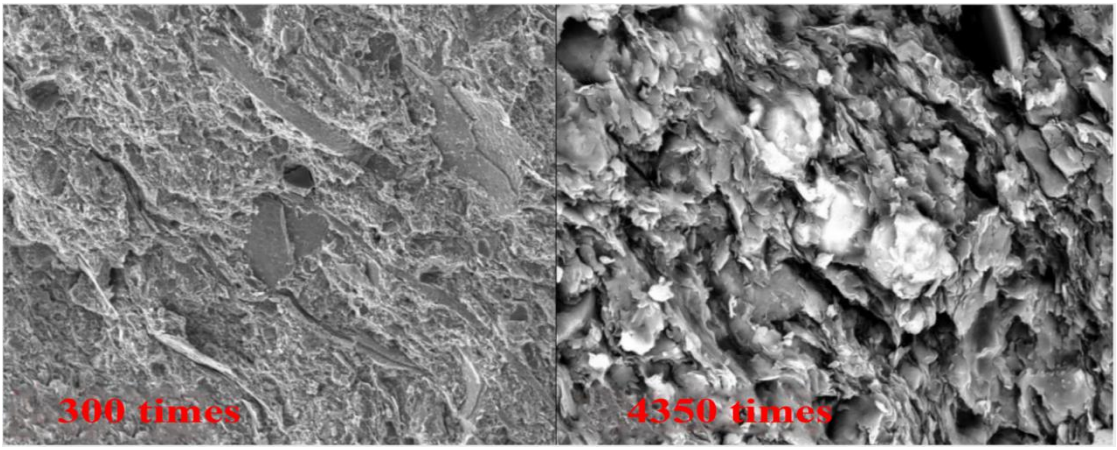

Fig. 2.7(c) Scanning electron microscopic image of the shale sample numbered 3

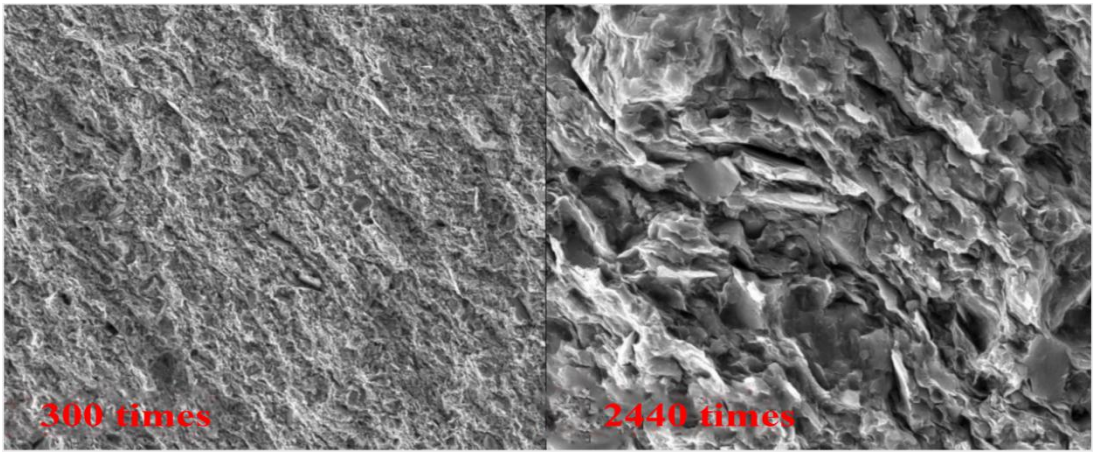

Fig. 2.7(d) Scanning electron microscopic image of the shale sample numbered 4

2.4. Hydrating properties of mud shale

In production practice, it is recognized that both the density and performance of a drilling fluid will have a great impact on borehole stability, which, as discussed, is mainly caused by the complex physical and chemical effects of the mud shale's contact with the drilling fluid. The sensitivity of different types of mud shale to a drilling fluid is different, and the influence on borehole stability changes with it. Therefore, it is necessary to recognize the physical and chemical properties of hard

brittle mud shale, including its hydration and expansion. Hydration expansion of mud shale is usually measured by cation exchange capacity (CEC). CEC values reflect the water absorption capacity of mud shale. Greater CEC indicates easier hydration. CEC is also associated with clay dispersion and increases with clay dispersion. Using the methylene blue method, a CEC value of shale was determined.

2.4.1. Methylene blue method

To begin, the mud shale samples processed by 100 mesh screens are dried at 105±3℃ for 4h. 100g of dry rock powder are picked, and distilled water is added to a total volume of 200mL. High-speed stirring then takes place for 15 minutes on a five-axis mixer. Using a needle-free syringe to measure 2.0mL, the mud magma solution is shaken into a conical bottle containing 10mL of water. 15mL of 3% a hydrogen peroxide solution is added. 0.5mL 2.5mol/L sulfuric acid solution is then boiled slowly for 10 min (not dry) and then diluted to 50mL with water. 0.5mL 0.01mol/L of methylene blue solution is added to the conical bottle each time and rotated for 30s. When in a solid suspension state, a drop of liquid is taken with a stirring rod and placed on a piece of filter paper. When the dye shows a blue ring around the dyed solid, the titration end point is reached, and when the blue ring expands outward from the spot, the conical bottle is then rotated for 2 min. Another drop is placed on the filter paper. If the blue ring is still obvious, then it has reached the end. The CEC is ultimately calculated from the volume of consumed methylene blue solution.

2.4.2. Experimental results

The mud shale cuttings from well A-1 in Indonesia's Oilfield A were selected as experimental samples. The results are shown in Figure 2.8. The CEC value of the Cisubuh formation is the highest, up to 20.5meg/100gram, with an average 16meg/100gram. The next is the Parigi formation, with an average of 11meg/100gram. The last is the Cibulakan Atas formation, with an average of 8meg/100gram. The CEC values of Cisubuh and Parigi range from 11 meg/100g to 20.5meg/100g, which indicates that shale in Cisubuh has the ability to absorb water, hydrate, and expand. If it is exposed to drilling mud for a long time, the borehole is more likely to collapse. The Cibulakan Atas formation, with 3<CEC<10, belongs to hard mud shale with a moderate dispersion and spalling trend. The results show that the mud shale in the entire well section has weak hydration or non-hydration properties, but because of its hard brittleness, its micro fractures are relatively developed.

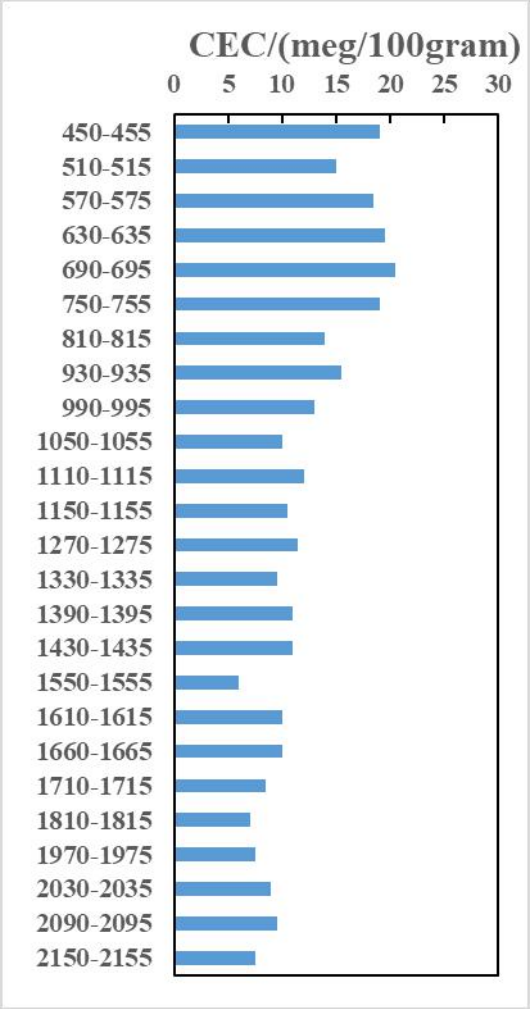

Fig. 2.8 CEC values of mud shale in well A-1

2.5. Mechanical properties of mud shale rocks

The deformation characteristic of rock is an important mechanical characteristic. It refers to a change in the shape and size of rock under the influence of physical factors. In a sense, the deformation of rock will directly affect normal engineering practices. If there is enough understanding of the law of rock deformation characteristics, the correct mathematical expressions can be used to first describe these deformation characteristics. These expressions can then be further used to calculate deformation produced under external loads, which, in turn, allows us to

better evaluate the rock's stability[51].

The deformation characteristics of rocks can usually be obtained from the stress-strain curves recorded during laboratory tests. A stress-strain curve of rock reflects the corresponding strain law at various stress levels. Figure 2.9 shows a typical rock stress-strain curve under uniaxial compression. According to the change in the shape of a stress-strain curve, the deformation of rock can be divided into the following stages:

(1) OA Stage: Usually called the compaction stage, it is characterized by the concave shape of a stress-strain curve. That is, the increment of strain decreases with a corresponding increase in stress. The main reason for this characteristic is the closure of micro-fractures in the rock under an external force.

(2) AB Stage: This is an elastic stage in which a stress-strain curve is basically a straight line. The deformation can be restored after unloading, and the stress value corresponding to point B is called a ratio limit.

(3) BC Stage: This is a nonlinear elastic stage in which a stress-strain relationship is no longer a straight-line relationship, but it still belongs to the elastic stage. Before point C, the stress-strain relationship after unloading returns to the original state according to the original path. The stress value corresponding to point C is called yield stress.

(4) CD Stage: This is a plastic stage. When the stress value exceeds point C (yield stress), the stress-strain curve becomes concave with an increase in stress. This clearly shows the phenomenon of strain increasing, and it is at this stage that the rock

produces irreversible plastic deformation. The stress value corresponding to point D is called the peak strength. For hard rock, the plastic deformation appears very small, and this stage may not even exist.

(5) DE Stage: This is the post-peak stress-strain curve. Here, rock failure occurs after the peak strength (D), but the rock still has a certain residual strength.

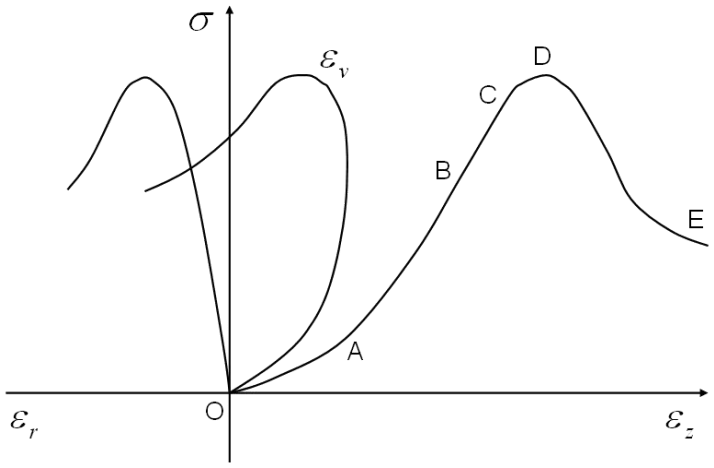

Fig. 2.9 Representative rock stress-strain curve

According to a stress-strain relationship of rock, its mechanical properties can be divided into elasticity and plasticity. Elasticity means that in a certain range of stress, the rock is deformed by external forces, and after removing the external forces, the rock is restored. Plasticity, on the other hand, refers to the phenomena in which stress exceeds the yield stress and deformation can continue without causing the rock to fracture. After removing the external forces, the rock can no longer be completely restored to its original form.

In addition, according to a relationship between rock deformation and failure, rock properties can be divided into brittleness and ductility. Brittleness refers to the property in which the deformation of rock results in breakage over a small period of

time. Conversely, ductility refers to the property in which the object can withstand large degrees of deformation without losing its bearing capacity. The ductility and brittleness of the material are divided according to: (1) the total strain before failure and (2) the slope drop of a negative slope on a full stress-strain curve. The total strain before failure is small, the steep negative slope is brittle, and vice versa.

In engineering, the total strain greater than 5% is classified as a ductile material, and lower than 5% will be classified as a brittle material. Heard[52] (1963) divided rocks into three categories, with 3% and 5% as limits: If the total strain is less than 3%, it is brittle rock; if the total strain is 3%~5%, it is semi-brittle rock; finally, the total strain greater than 5% is classified as ductile rock. The ductility and brittleness of rock are relative characteristics, and both can be transformed into each other under certain conditions. For example, normal temperature and atmospheric pressure on brittle rock can lead to high ductility when exposed to both high temperature and pressure.

Because a core taken from a site is irregular in shape and cannot be directly used in experiments, it needs to be processed indoor. During the processing of a core column, the two ends of a cylindrical specimen are smooth and polished, so that the aspect ratio of the rock sample is 1.8 - 2.0.

2.5.1. Uniaxial and triaxial compressive strength tests

A three-axis strength test device used is produced by the American MTS Company. The structure diagram is shown in Figure 2.10.

Fig. 2.10 Rock triaxial test apparatus

The device consists of five main parts: a high temperature and high pressure triaxial chamber, a confining pressure system, an axial pressure system, a heating and constant temperature system, and finally a data acquisition and control system. The design index of the triaxial chamber is confined to 200MPa pressure, which can accommodate 50mm diameter rock samples. The internal design of the autoclave can compensate for the confining pressure of the system during the loading process, and the top force of the plunger produced by the confining pressure can be offset by itself. Therefore, the longitudinal pressure of the machine on a rock sample is equal to the differential stress of the rock sample in a triaxial experiment, with a convenient operation system. Both the confining and axial pressure of the triaxial chamber are controlled by an electro-hydraulic servo. The axial, transverse strain and axial load of a rock sample are measured by the sensor installed in the autoclave. A data signal is

transmitted to TESTSTAR an automatic acquisition control system, which accomplishes several functions including automatic data acquisition, storage, processing and the drawing of stress-strain curves.

2.5.2. Test results of uniaxial and triaxial compressive strength

As has been discussed, the core under study in this thesis is made up of mud shale from Indonesia's Oilfield A, and the coring depth of the sample is approximately 1302-1312m. The cores before and after uniaxial and triaxial compressive strength tests are shown in Figure 2.11 and Figure 2.12. Likewise, the uniaxial and triaxial stress-strain curves are shown in Figure 2.13 and Figure 2.14. It is found that the failure modes of mud shale mainly relate to splitting failures and single shear failures. Under uniaxial compression, splitting failures are the primary form of failure, but single shear failures occur mainly under triaxial compression.

The experimental results show that the uniaxial compressive strength of the core is 6-35MPa. Under confining pressure, the compressive strength of the core increases, and the total compressive strength is above 40 MPa under a corresponding 10-30 MPa confining pressure. The elastic modulus under uniaxial conditions is 2-10GPa, and Poisson's ratio is about 0.20-0.27. The test core, whether under uniaxial or triaxial conditions, shows that the rock's stress decreases rapidly after exceeding the peak strength, which indicates that the rock has strong brittleness characteristics. In addition, with an increase in confining pressure, the failure strength of the test core also increases, and the deformation characteristics of the rock show the transition

from brittleness to plasticity under low confining pressure.

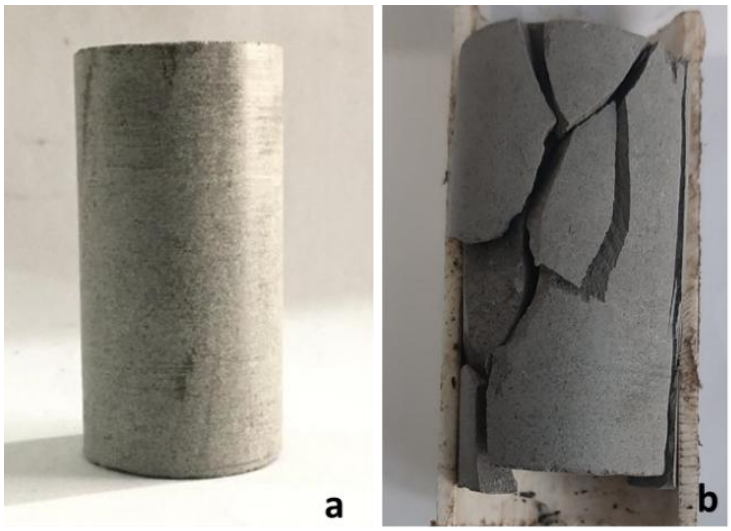

Fig. 2.11 Uniaxial compressive strength test cores: (a) before the test and (b) after the test

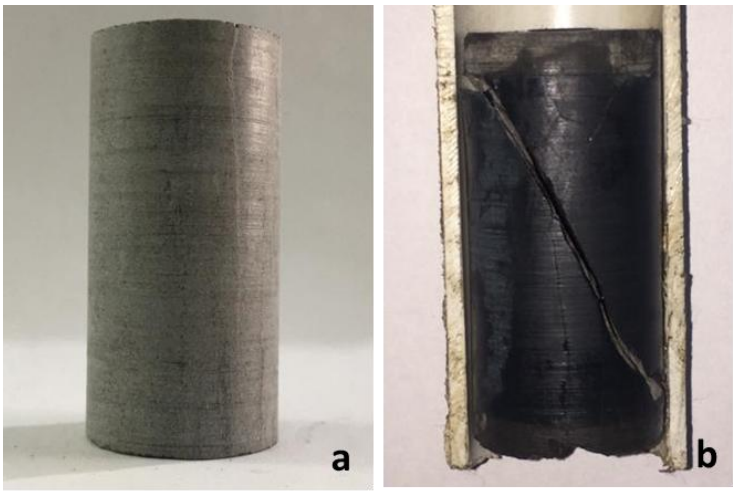

Fig. 2.12 Three-axis compressive strength test core: (a) before the test and (b) after the test

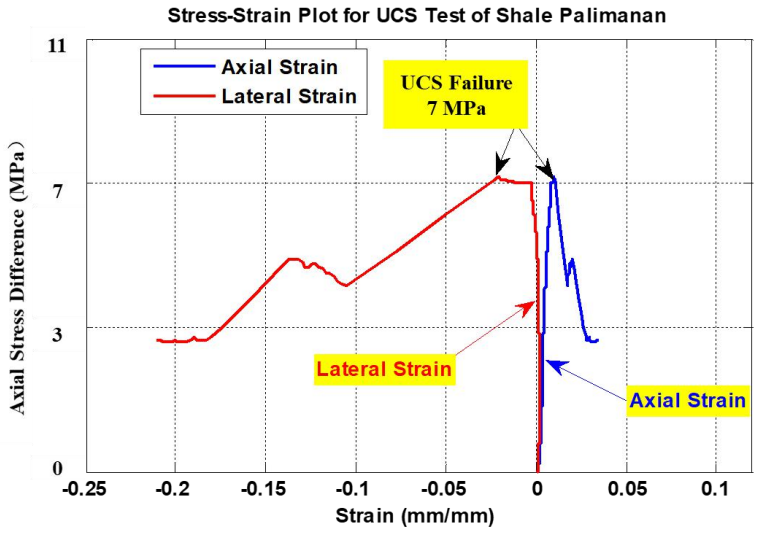

Fig. 2.13 Stress-strain plot for UCS test of mud shale

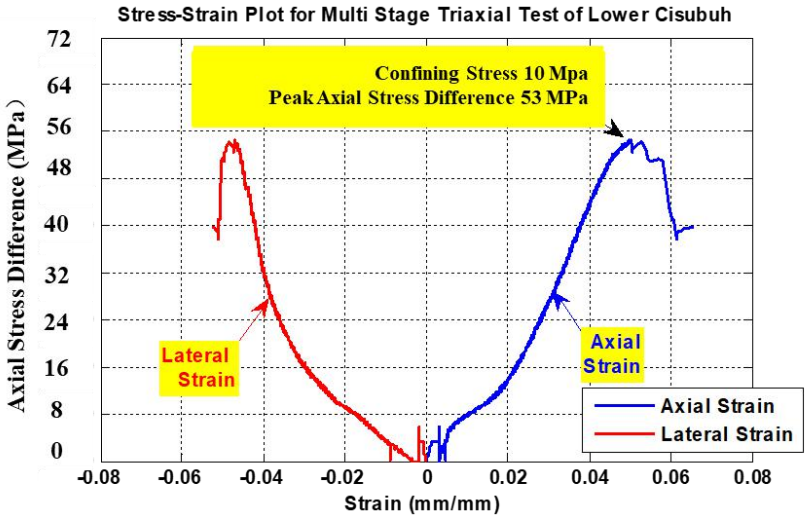

Fig. 2.14 Stress-strain plot for multi stage triaxial test of mud shale

2.5.3. Mol-Coulomb analysis

The compressive strength of rock will change with a corresponding change in confining pressure. Using the Mohr-Coulomb strength criterion, a linear variation of compressive strength under an increase in confining pressure can be approximated. Using the compressive strength data of several different confining pressures, two important parameters for the compressive shear failure of the characteristic rock can

be calculated: cohesion and an internal friction angle. The Mohr-Coulomb criterion expressed by the principal stress is:

$$\sigma_1 = \sigma_3 \cot^2\left(\frac{\pi}{4} - \frac{\phi}{2}\right) + 2C\cot\left(\frac{\pi}{4} - \frac{\phi}{2}\right) \quad (2\text{-}1)$$

In the formula:

C: Cohesive strength, MPa;

φ: Internal friction angle, radian;

σ_1: Maximum principal stress, MPa;

σ_3: Minimum principal stress, MPa.

Based on the experimental results which showed the rock's compressive strength at different confining pressures and at similar depths, the cohesion and internal friction angle can thus be calculated using the Mohr-Coulomb criterion. According to the Mohr-Coulomb criterion, shale cohesion is between 2-9MPa, the internal friction angle is about 41°, and the shear failure resistance is poor.

2.5.4. Tensile strength tests

Tensile strength is one of the most important indexes of rock mechanical properties. When it comes to rock materials, it is difficult to load tensile stress directly on an axis, so an indirect method is generally used to measure tensile strength in indoor experiments. In this thesis, the indirect tensile strength of rock samples is accomplished through a rock splitting method, also known as the Brazil splitting method. This method is recommended by the Laboratory Committee of the International Rock Society and is used to determine the tensile strength of rock

samples. According to the Brazilian splitting experiments, disc-shaped rock samples, about 25mm in diameter and about 10 mm in thickness, are used. About 10mm of a rock sample is then intercepted from one end on the basis of the processed compressive strength of the experimental rock samples for the Brazilian splitting experiment. It can be proven by the elastic theory that the tensile strength of the cylindrical specimen, when split under radial tensile stress, is determined by the following formula:

$$S_t = \frac{2P_u}{\pi Dt} \tag{2-2}$$

In the formula:

P_u: Load during specimen failure, N;

D: Diameter of cylinder specimen, m;

t: Thickness of cylinder specimen, m.

Based on the mud shale core from Indonesia's Oilfield A, the tensile strength tests for the three rock samples obtained through the Brazilian disk splitting method were completed. The photos of the rock samples before and after the experimental failure are shown in Figure 2.15, and the experimental data and tensile strength calculation results are shown in Table 2.4. The tensile strength is basically between 0.5-3MPa. Compared with the uniaxial compressive strength data, it is found that the uniaxial compressive strength is about 12 times that of the tensile strength.

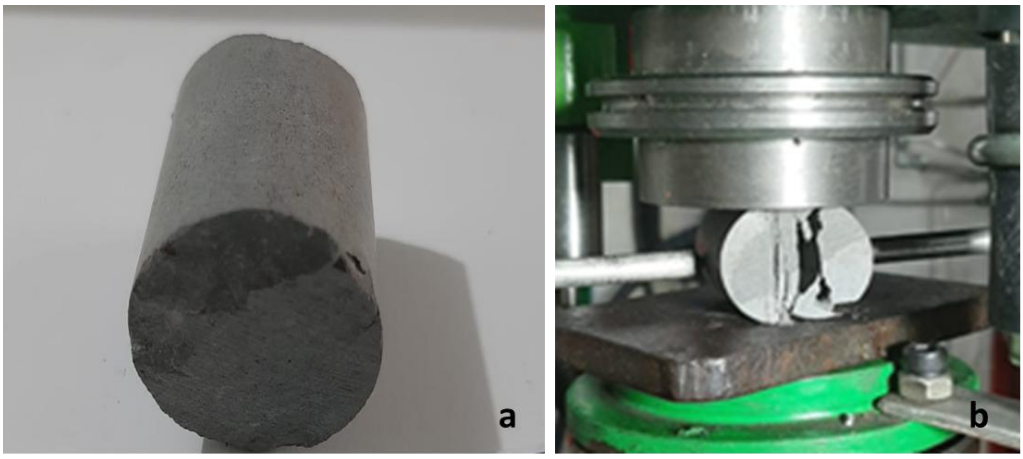

Fig. 2.15 Tensile strength experiment: (a) before the test and (b) after the test

Table 2.4 Experimental data on tensile strength of shale

No.	Diameter (mm)	Thickness (mm)	Failing load (N)	Tensile strength (MPa)
1	25.13	12.41	1247	2.55
2	25.24	13.88	263	0.48
3	25.17	14.44	1700	2.98

2.5.5. Establishment of an empirical model for finding formation elastic parameters from logging data

Using multipole array acoustic logging (XMAC) a longitudinal wave time difference (DTCO) and a shear wave time difference (DTSM) in the Cisubuh, Parigi, Cibulakan Atas and the MMC formations in Oilfield A are obtained. Through formula (2-3) and formula (2-4), the longitudinal wave velocity V_p and the shear wave velocity V_s are calculated. Based on an intersection diagram, a relationship between the two is obtained. As shown in Figure 2-16, the relationship between V_p and V_s is fitted in formula (2-3).

$$V_P = 304800 / DTCO \tag{2-3}$$

$$V_S = 304800 / DTSM \tag{2-4}$$

$$V_S = 2035.2 \ln^{V_P} - 14793 \tag{2-5}$$

where DTCO is a longitudinal time difference, us/ft; DTSM is a transverse wave difference, us/ft; V_p is the longitudinal wave velocity, m/s; V_s is the transverse wave velocity, m/s.

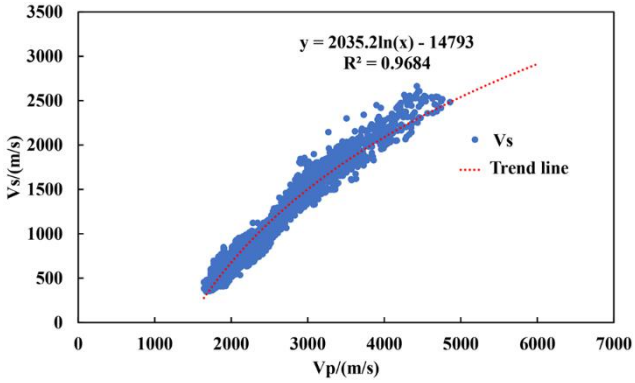

Fig. 2.16 The intersection diagram of longitudinal wave velocity V_p and shear wave velocity V_s

A relationship between the dynamic elastic parameters and the longitudinal and wave equations and a relationship between the dynamic elastic parameters and the longitudinal velocity can be deduced:

$$E_d = \frac{\rho v_s^{\,2}(3v_p^{\,2} - 4v_s^{\,2})}{(v_p^{\,2} - 2v_s^{\,2})} \tag{2-6}$$

$$\mu_d = \frac{(v_p^{\,2} - 2v_s^{\,2})}{2(v_p^{\,2} - v_s^{\,2})} \tag{2-7}$$

where

E_d: Dynamic modulus of elasticity, GPa;

μ_d: Dynamic Poisson's ratio;

ρ: Density, g/cm3.

As determined by the longitudinal and transverse wave velocities, the dynamic elastic modulus and dynamic Poisson's ratio reflect the mechanical properties of a formation under instantaneous loading, which is not consistent with the static load of the formation. Therefore, it is necessary to establish a correlation between the dynamic and static parameters to further obtain the static parameters. The static elastic modulus and Poisson's ratio can be obtained by an indoor rock mechanics experiment, and a conversion relationship can then be seen by comparing the dynamic and static elastic parameters. A comparison between the static deformation parameters obtained by an uniaxial compressive strength experiment and the dynamic parameters obtained by acoustic velocity calculations is shown in Figures 2.17 and 2.18. According to the experimental results, the empirical formulas for the conversion of static and static parameters obtained by fitting the experimental results are as follows:

$$E_s = 0.3386E_d + 2.3983 \tag{2-8}$$

$$\mu_s = 0.4498\mu_d + 0.0881 \tag{2-9}$$

where

E_s: Static elastic modulus, GPa;

μ_s: Static Poisson's ratio.

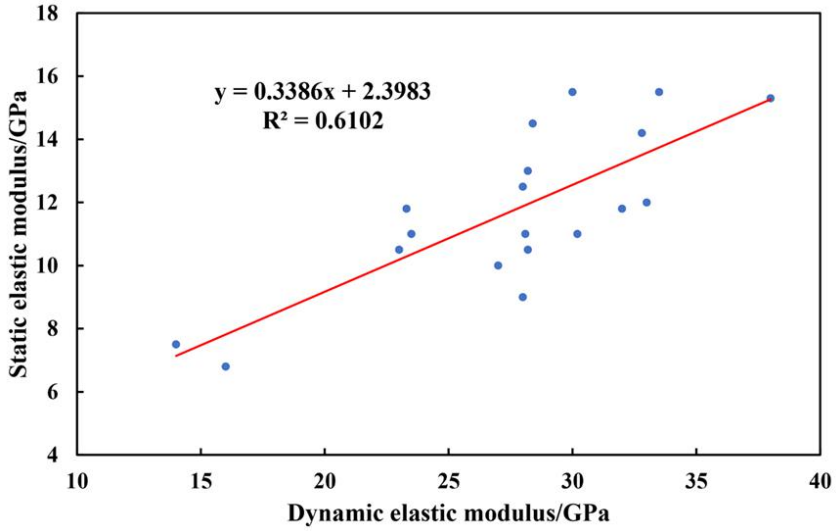

Fig. 2.17 Comparison of dynamic and static elastic modulus and fitting formula

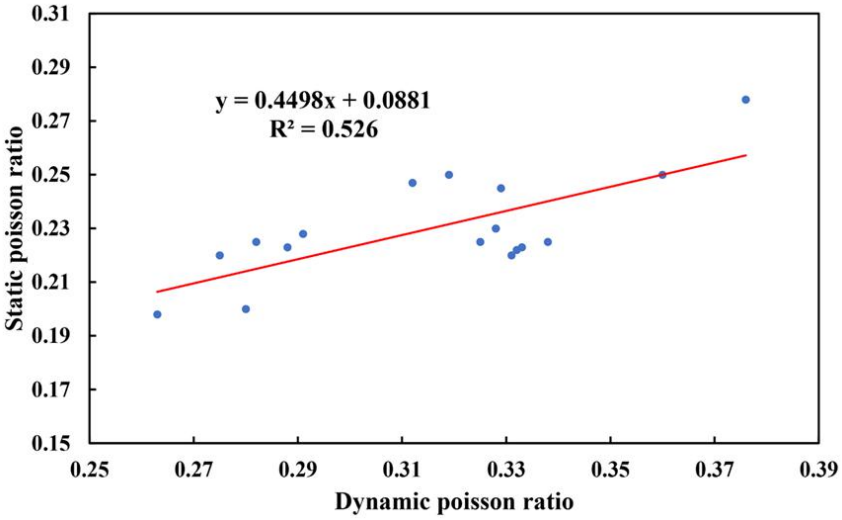

Fig. 2.18 Comparison of dynamic and static Poisson's ratio and its fitting formula

2.6. Chapter conclusions

1. The mineral composition, microstructure, hydration and expansion characteristics of mud shale found in Indonesia's Oilfield A were analyzed by X ray diffraction, electron microscope scanning and methylene blue experiments.

The experimental samples contain rock material from the Cisubuh, Parigi, and Cibulakan Atas formations. The Cisubuh formation has the highest clay mineral

content, up to 30.6%, followed by the Parigi formation at 22.3%, and finally the Cibulakan Atas formation at 15.3%. In general, the clay content of all three formations is not especially high, but all of them contain montmorillonite, which means that the formations have strong water absorption and expansion properties. The content of montmorillonite in the Parigi formation was the highest at 8.0%, followed by the Cisubuh formation at 6.6%, and finally the Cibulakan Atas formation at 4.2%.

The mud shale found in Oilfield A is relatively dense, but there are hole seams between the grains, with a width of about 5-10 μm. Some samples are filled with calcite between muds, and an illite-montmorillonite mixture is either layered or flaky. Both the layered structure and intergranular hole joints are conducive to drilling fluid seepage and thus have adverse effects on borehole stability.

The Cisubuh mud shale has a certain ability to absorb and expand. If this mud shale is exposed to drilling mud for a long time, a borehole is more likely to collapse. The Cibulakan atas formation, with 3<CEC<10, belongs to a hard mud shale with moderate dispersion and spalling trends. The mud shale in the whole well section, therefore, has weak hydration or non-hydration properties, but because of its hard brittleness, micro fractures are relatively developed.

2. The experimental results show that the uniaxial compressive strength of the core is between 6-35MPa. Under confining pressure, the compressive strength of the core increases, leading to a compressive strength above 40 MPa when under 10-30MPa of confining pressure. The elastic modulus under uniaxial conditions is 2-10GPa, and Poisson's ratio is about 0.20-0.27. According to the Mohr-Coulomb

criterion, shale cohesion is between 2-9MPa, the internal friction angle is about 41°, and shear failure resistance is poor. Compared with uniaxial compressive strength data, it is found that the uniaxial compressive strength is about 12 times that of the tensile strength.

Under uniaxial compression, splitting failure frequently occurs, while single shear failure occurs mainly under triaxial compression. The experimental results show that the uniaxial compressive strength of the core is between 6-35MPa. Under confining pressure, the compressive strength of the core increases, and the compressive strength is above 40 MPa when under 10-30 MPa of confining pressure. The elastic modulus under uniaxial conditions is 2-10GPa, and Poisson's ratio is about 0.20-0.27. The test core, whether under uniaxial or triaxial conditions, shows that the rock stress decreases rapidly after exceeding its peak strength, which indicates that the rock has strong brittleness characteristics. In addition, with an increase in confining pressure, the failure strength of the test core increases, and the deformation characteristics of the rock show a transition from brittleness to plasticity under low confining pressure.

CHAPTER III. Study on 3D Geomechanics Modeling Methods for Mud Shale Formations

Borehole collapse or rupture is a physical phenomenon caused by crustal stress exceeding the corresponding rock strength. Borehole stability analysis or design calculates the changing crustal stress conditions near a well and compares these conditions with the rock's strength. This requires a structural geomechanical model. Using a micro fracture test or DFIT (diagnostic fracture injection test), crustal stress and pore pressure in a study area can be accurately measured. A small amount of measured data can then be obtained to constrain the established geomechanical models. A complicating factor in this is the reality that pore pressure measurements in shale are usually difficult to obtain. However, an accurate calculation of crustal stress can also correct the pore pressure data obtained by drilling data.

Through a series of core tests, well logging data and seismic inversion data, the mechanical parameters in the study area are described in detail. Spatial distributions of the 3D elastic modulus, Poisson's ratio and pore pressure in the target oilfield are established. A 3D geomechanical model with heterogeneity, porosity and elastoplasticity is also established. Adding to this, a 3D stress distribution and a 3D safety density window for the target oilfield are also calculated using the finite element method. Through LOT data from the drilling well, the complex conditions of the drilling process and the data obtained through drilling completion, the geomechanical model is validated. Finally, the well location arrangement, trajectory optimization, casing design and drilling completion management in the study area are

managed by the 3D crustal stress model and density window model. The flowchart is shown in Figure 3.1.

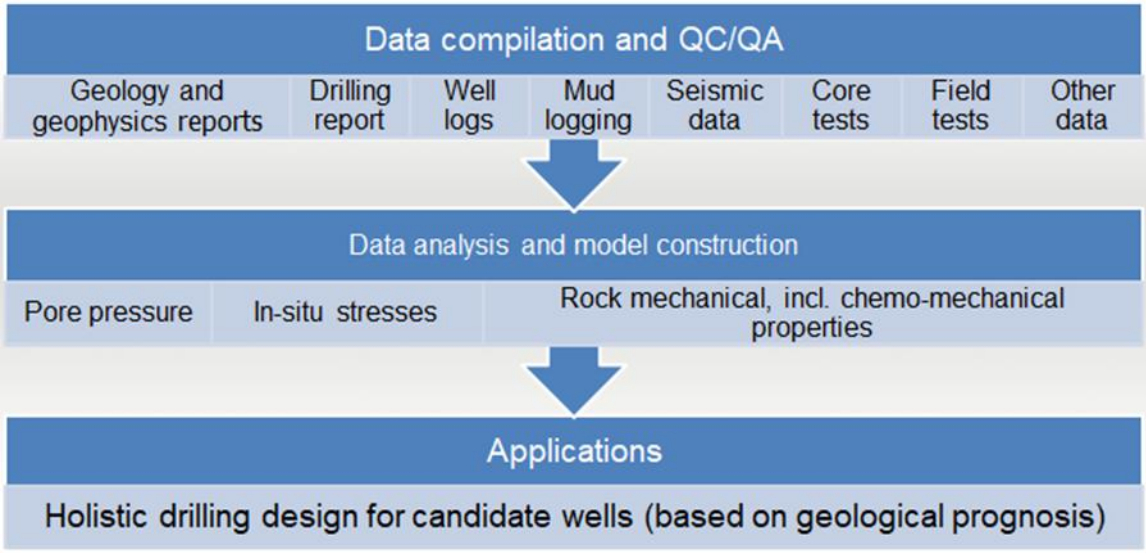

Fig. 3.1 Flowchart of integrated geological engineering technology

3.1. Modeling process

This work is based on the Petrel software platform, and the entire modeling process is shown in Figure 3.2. Firstly, based on the interpretation of seismic data, a tectonic surface of the study area is obtained, and a geological model which can truly reflect the structural changes is generated. Then, a 3D elastic modulus, 3D Poisson's ratio and other 3D heterogeneous material properties are established, and ultimately a 3D pore pressure model is generated. By assembling the 3D geomechanical model and using the heterogeneous-pore-elastic-plastic model to calculate the 3D crustal stress, a 3D crustal stress distribution is finally obtained, and limited measured values are used to control the 3D crustal stress results.

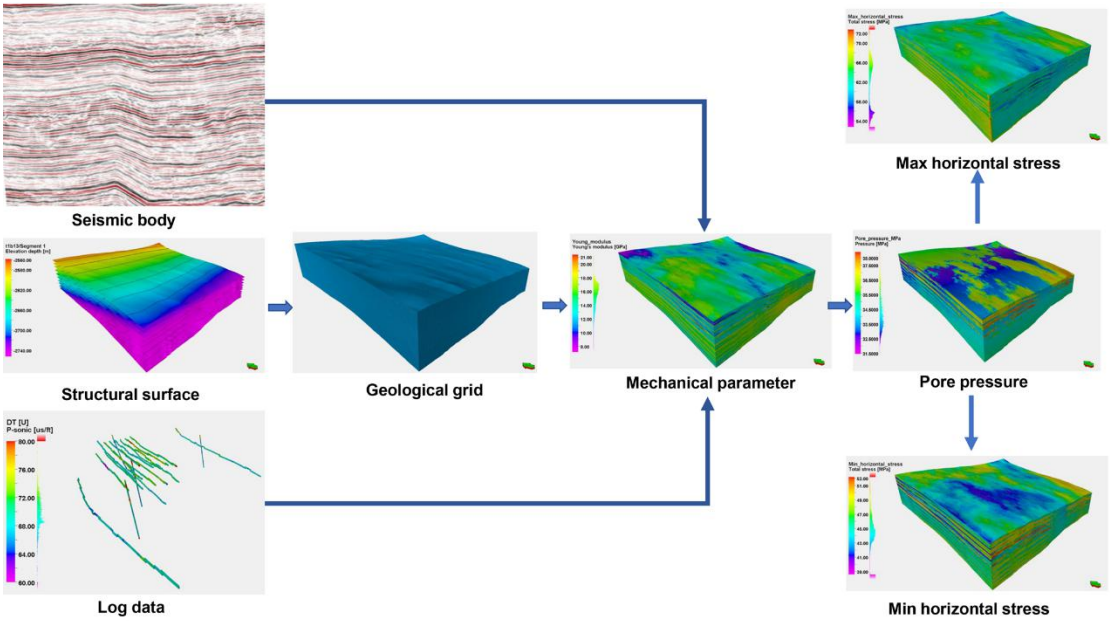

Fig. 3.2 Flowchart of 3D crustal stress modeling

3.2. 3D geomechanical model

Compared with the research area, the drilling data is still relatively minimal. In order to obtain the fine 3D mechanical parameter model and the 3D pore pressure model, it is necessary to use interpolated data from the existing wells. However, the mud shale stratum belongs to heterogeneous strata. Conventional linear interpolation and sliding average interpolation, therefore, cannot produce an accurate 3D mechanical model. Because the rock's mechanical parameters are mainly controlled by lithofacies factors, mechanical modeling must be carried out under the constraints of indoor test results by means of logging and seismic inversion data.

Both a meticulous 3D longitudinal wave velocity and a 3D shear wave velocity are obtained at the core of various 3D rock mechanical parameters modeling. It is necessary to make full use of logging data and seismic data to carry out 3D geomechanical modeling. Therefore, the 3D seismic interval velocity body in the

study area is obtained by seismic wave inversion. Based on the Kriging interpolation method[53], the well-drilled interval velocity (V_p) data in the model area is interpolated in 3D. The meticulous 3D interval velocity model in the study area is then obtained by using the 3D seismic interval velocity to constrain the interpolation results. Next, 3D rock mechanics parameters and 3D pore pressures are obtained by various empirical formulas. A 3D stress distribution in the target oilfield is calculated by the finite element method.

3.2.1. Kriging interpolation methods

By using the Kriging interpolation method, a 3D interval velocity in the study area is obtained, and then a 3D distribution of various mechanical parameters is calculated. Kriging is a random simulation method of geostatistics, which generates a continuous normal distribution through an iterative method. It is based on a variable estimation of a variation function, which takes into account a spatial distribution position relationship between sampling points and the structural information between variables. The Kriging method was first established by the South African mining engineer D.G. Krige in view of the characteristics of gold grade combined with geological estimation. It was then perfected by French mathematician Georges Matheron to form a complete theoretical system. Based on the idea of geostatistics, the Kriging method calls an attribute of a continuous change in space a "regional variable", and uses both a covariance function and a semi-variant function to describe a variation law of the regional variable. A mathematical model from the Kriging

interpolation is as follows: the Kriging method is a local estimation method, which usually uses a set of measured data and its corresponding spatial structure information to obtain a 3D spatial distribution of attributes. For a heterogeneous texture stratum it has excellent modeling accuracy. The principle of the algorithm is as follows:

A trend control model is:

$$E[Z(u)] = a_0 + a_1 y(u) \tag{3-1}$$

where $y(u)$ is a secondary variable, and it reflects a spatial trend of Z variables (corresponding to two parameter a_0 and a_1). Letter u indicates data points of coordinates.

A Kriging estimate:

$$Z^*_{KT}(u) = \sum_{\alpha=1}^{n} \lambda_\alpha^{KT}(u) Z(u_\alpha) \tag{3-2}$$

where $\lambda_\alpha^{KT}(u)$ is a weighting factor.

The Kriging equations:

$$\left\{ \begin{array}{c} \sum_{\alpha=1}^{n} \sum_{\beta=1}^{n} \lambda_\beta^{KT}(u) C_R(u_\beta - u_\alpha) + \mu_0(u) + \mu_1(u) y(u_\alpha) = C_R(u - u_\alpha) \\ \sum_{\beta=1}^{n} \lambda_\beta^{KT}(u) = 1 \\ \sum_{\beta=1}^{n} \lambda_\beta^{KT}(u) y(u_\beta) = y(u) \end{array} \right\} \tag{3-3}$$

Among them, $\mu(\ )$ is the Lagrange parameter and $C_R(\ )$ is the residual covariance function.

The principle of finding a 3D interval velocity is as follows: Based on the drilling V_P data as the main variable, a 3D seismic interval velocity is taken as the secondary variable. Using the spatial structure information provided by a variogram model to solve the Kriging equation set, we calculate the weighting coefficient $\lambda_\alpha^{KT}(u)$. The weighted linear estimate is then carried out to obtain a required 3D

interval velocity value, or the estimated value $Z_{KT}^{*}(u)$.

3.2.2. 3D pore pressure

Formation pore pressure refers to the pressure of a rock's pore fluid. As a geological parameter, pore pressure plays an important role in oil and gas exploration, drilling engineering, and oil and gas development. As far as drilling engineering is concerned, pore pressure is an essential and important parameter to realize rapid, safe and economical drilling, so accurate prediction of pore pressure is crucial. During drilling, the DC index (a drilling pressure index corrected by a drilling fluid density) method, the mechanical specific energy method and real-time monitoring can be used. Drilling Stem Test (DST) technology can also be used to measure formation pore pressure in situ during drilling. However, the measurement data for a whole well is inconsecutive. Thus, pore pressure can instead be continuously estimated based on petrophysical data such as *P*-wave propagation time.

In drilling practice, the actual formation pressure is greater or less than the hydrostatic column pressure, i.e., the abnormal pressure phenomenon. The formation pressure exceeding the normal formation hydrostatic pressure is called abnormal high pressure, while the formation pressure that is below the normal formation hydrostatic pressure is called abnormal low pressure. Abnormal pressure is a global phenomenon and has been found in many basins in the world. In the global investigation of hydrocarbon resources on land and at sea, abnormal formation pore pressure has been encountered. Abnormal pressure can occur in shallow depths underground, only a few

hundred meters, or more than 6000 meters deep. It can also exist in mudstone-sandstone series or in block evaporite-carbonate sections. In terms of an geological age, the formations that often demonstrate this abnormal pressure encompass the Pleistocene to Cambrian epochs.

At present, the formation mechanisms responsible for abnormal formation pressure are classified as follows:

(1) Variation of a pore volume of rock: vertical load (under compaction); lateral structural loading; secondary cementation;

(2) Change of a pore fluid volume: temperature change; mineral transformation; hydrocarbon generation; hydrocarbon thermal degradation; fluid (mainly gas transport);

(3) Fluid pressure (hydrodynamic head pressure) variation and fluid flow: osmotic action; fluid pressure head; oilfield exploitation; permafrost environment; relative density differences (e.g., between gas and oil).

3.2.2.1. Formation mechanism of abnormal high pressure in strata

Formation pore pressure refers to the pressure of a rock pore fluid. As a geological parameter, pore pressure plays an important role in oil and gas exploration, drilling engineering and oil and gas development. At present, the accepted pressure forming mechanisms can be divided into two categories: under compaction and non-under compaction. Under compaction means that in the process of formation compaction, the fluid will be intercepted in pores because of a fast deposition speed

and poor formation permeability, thus supporting a part of the increasing vertical load forming mode. This method accords with a loading curve.

Non-under compaction usually includes a pore fluid volume change, a fluid pressure change, fluid flow, formation tectonic movement and fluid density difference. In this case, the two mechanisms of a pore volume change - fluid pressure change and fluid flow - accord with an unloading curve. The classification of the above pressure forming mechanism is shown in Table 3.1.

1. Volume change of a pore fluid

The volume change of a pore fluid can be divided into a ground temperature rise, mineral transformation, hydrocarbon generation and fluid migration.

The increase in ground temperature: An increase in temperature alongside an increase in buried depth makes the expansion of pore water larger than that of rock (the coefficient of thermal expansion of water is greater than that of rock). If pore water cannot escape due to the existence of a fluid barrier, the pore pressure will increase.

Mineral conversion: When minerals are converted into sediments, side water is released, a fluid volume increases, and abnormal high pressure is produced, such as montmorillonite dehydration, and gypsum conversion to anhydrite dehydration. The transformation of montmorillonite and illite is the main example of this transformation. The deposited montmorillonite adsorbs free water between grains and results in bound water between clay layers. When the local temperature reaches about 123 degrees centigrade, the lattice of a clay structure breaks down. The interlayer

bound water of montmorillonite is excluded and becomes free water - a process known as the dehydration of montmorillonite - and the corresponding buried depth is referred to as the dehydration depth of montmorillonite. The bound water released into pores expands and its volume far exceeds the volume reduced by the lattice destruction. If the drainage is smooth, the formation is further compacted and the pore pressure is hydrostatic. If the formation is closed, the formation pore pressure above the hydrostatic pressure will be produced. If there is potassium ion, more specifically adsorption potassium ion, the montmorillonite will transform to illite.

Hydrocarbon generation and fluid transport: During a gradual buried depth process, a reaction involved in converting organic matter into hydrocarbons also produces an increase in fluid volume, resulting in overpressure in a single pressure storage box. Many studies have shown that the fractures of overpressure associated with hydrocarbon generation are the mechanism of hydrocarbon migration from source rock to porous, high permeability reservoir rock. Methane generation, in particular, has been cited as the cause of overpressure generation in many reservoirs. Gas is typically associated with abnormal pressure, which is further characterized by gas saturation. When the organic matter in the source rock or the oil entering the reservoir is converted to methane, a considerable volume increase is caused. These volume increases can produce strong ultrahigh pressure under closed well conditions.

2. Fluid pressure change and fluid flow

This kind of non-compaction pressure forming mechanism mainly includes osmotic action and fluid pressure head.

Osmosis: Osmosis is the migration of water with lower salinity to higher salinity through a semi-osmosis diaphragm. As long as the salt concentration on both sides of clay or shale varies significantly, the clay or shale acts as a semi-permeable membrane and produces osmotic pressure. The osmotic pressure difference is proportional to a concentration difference. Therefore, the greater the concentration difference, the greater the osmotic pressure difference. Because of this, concentration flow can produce high pressure in a closed area. The abnormal high pressure caused by osmosis is much smaller than that caused by compaction and hydrothermal action.

Fluid pressure head: Under the condition of self-flow or because of the existence of a permeable channel between a shallow layer and a deeper high-pressure layer, the pore pressure can be higher than the normal value. This situation is often encountered when drilling at the foot of a mountain.

3. Stratigraphic tectonic movement

Stratigraphic tectonic movements include formation uplift, structural shear stress and tectonic crustal stress loading.

Stratigraphic uplift: Because of the movement of strata, the deep strata are raised to a shallower depth, which leads to abnormal formation pressure in this part of the strata. During the formation of this pressure, the pressure of overlying strata decreases due to the stripping of the upper strata, which makes the strata unload and accord with an unloading curve.

Structural crustal stress loading: A pore structure can also withstand triaxial stress, but the situation of "shear stress strengthening, pore collapse" also occurs.

Especially in inverse or translational faults, vertical stress is not the maximum principal stress, and horizontal stress should always be considered. When the point of extreme failure is reached, the pore collapse leads to abnormal high pressure.

Structural shear stress: Structural shear stress also leads to shear failure in a pore space, which, in turn, leads to stress applied in the remaining dense pores and fluids, resulting in abnormal high pressure.

4. Difference in fluid density

A difference in hydrocarbon density, especially between water and gas, can produce abnormal pressure on top of hydrocarbon aggregation. The longer the hydrocarbon column, the greater the difference between the density of hydrocarbons and the surrounding water, and the greater the overpressure. Generally speaking, buoyancy differences can cause pressure to rise to hundreds psi order of magnitude.

Table 3.1 Abnormal High Pressure Compression Mechanisms

Abnormal High Pressure Mechanism		Compliance with unloading curve	Wave Speed Log	Density log
Change of pore volume of rock	Disequilibrium compaction	No	Reduce	Reduce
Volume change of pore fluid	earth temperature increase	Yes	Reduce	Not reduce or slightly elevate
	Mineral conversion			
	Hydrocarbon generation			
	Fluid (mainly gas) migration			
Fluid pressure variation	Osmosis	Yes	Reduce	Not reduce
fluid-flow	Fluid pressure head			
Stratigraphic tectonic movement	Formation uplift	Yes	Reduce	Not reduce
	Structural shear stress	No	Porosity is basically constant, not reflected	
	Structural stress loading			
Difference in fluid density	Difference in fluid density	No	Porosity is basically constant, not reflected	

3.2.2.2. Analysis of formation compression mechanism

The pore pressure prediction models commonly used are summarized and analyzed, as shown in Table 3.2. Different prediction models have their scope of application, and appropriate models should be selected for pore pressure prediction according to the formation of abnormal high pressure.

Table 3.2 Prediction of formation pore pressure

<table>
<tr><td colspan="2">Abnormal High-Pressure Mechanism</td><td colspan="2">Prediction model</td></tr>
<tr><td rowspan="3">Change of pore volume of rock</td><td rowspan="3">Disequilibrium compaction</td><td>Vertical method</td><td>Bryant; Alixant & Desbrandes</td></tr>
<tr><td>Horizontal Law</td><td>Eaton</td></tr>
<tr><td>Other methods</td><td>Simple method; Holbrook; Drauo; Bowers</td></tr>
<tr><td rowspan="4">Volume change of pore fluid</td><td>Increase in temperature</td><td colspan="2" rowspan="6">Bowers</td></tr>
<tr><td>Mineral conversion</td></tr>
<tr><td>Hydrocarbon generation</td></tr>
<tr><td>Fluid (mainly gas) migration</td></tr>
<tr><td>Fluid pressure variation</td><td>Osmosis</td></tr>
<tr><td>Fluid-flow</td><td>Fluid pressure head</td></tr>
<tr><td rowspan="3">Stratigraphic tectonic movement</td><td>Formation uplift</td></tr>
<tr><td>Structural shear stress</td><td colspan="2" rowspan="3">Analysis with geological condition</td></tr>
<tr><td>Structural stress loading</td></tr>
<tr><td>Difference in fluid density</td><td>Difference in fluid density</td></tr>
</table>

As shown, Figure 3.3 shows a relationship between acoustic delay and density logging of abnormal high pressure caused by loading. Because the loading accords with the rock loading law, the variation degree of acoustic delay and density is consistent. Figure 3.4 shows a relationship between acoustic delay and density logging caused by unloading. The sound velocity decreases greatly while density decreases slightly. An acoustic velocity reflects the conduction property of a rock, which, in turn, is affected by connection pores. The process of unloading results in an

increase in connection pores, so the acoustic velocity decreases. However, a bulk density reflects the rock volume property, which is affected by closed pores, and the elastic recovery of the closed pores is very small after unloading.

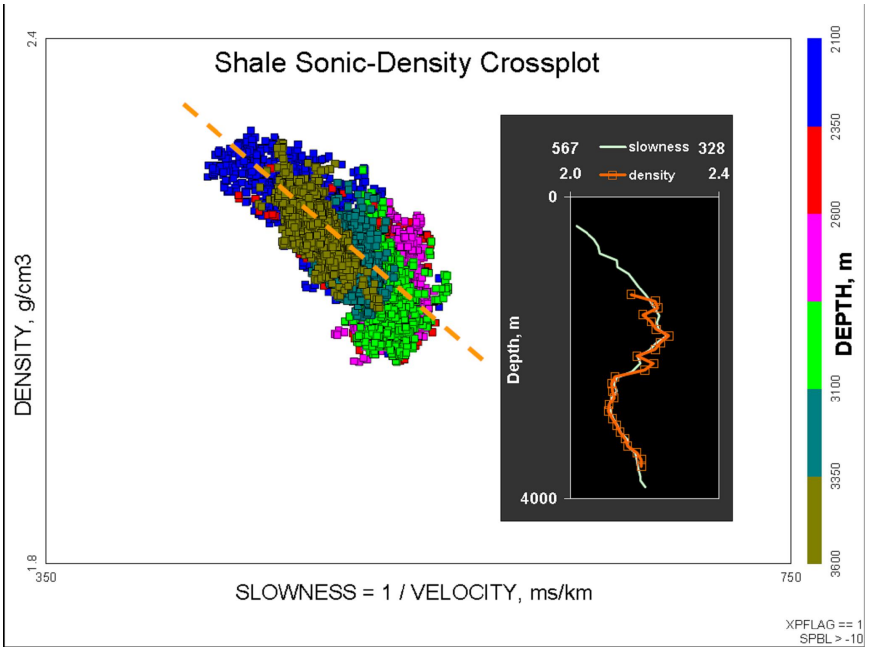

Fig. 3.3 Discrimination of Formation Mechanism of Loading Abnormal High Pressure

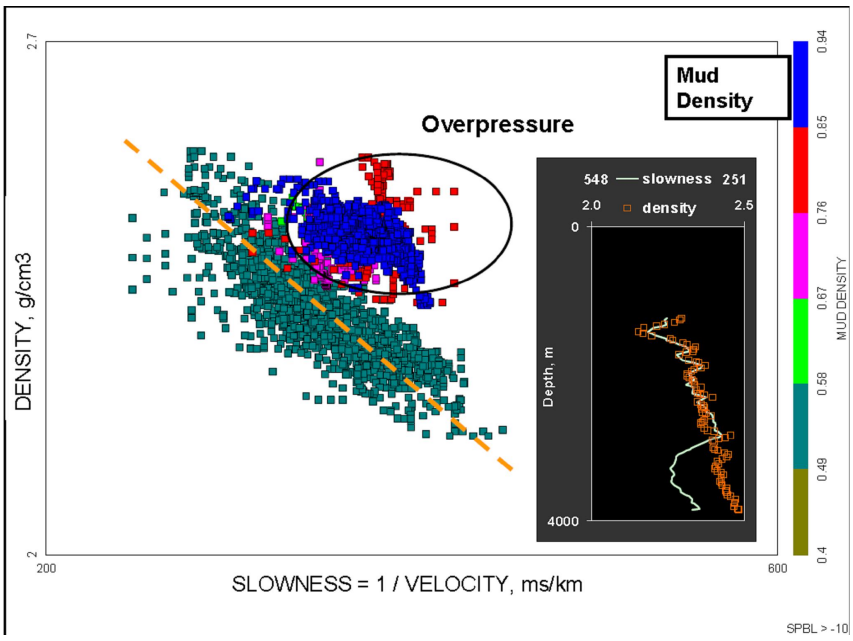

Fig. 3.4 Discriminating the Formation Mechanism of Unload Abnormal High pressure

3.2.2.3. Calculation method of pore pressure

The Eaton method is one of the most widely used quantitative methods in pore pressure prediction. Based on Eaton's experience and theoretical analysis in the Gulf of Mexico, a relationship between formation pore pressure and logging parameters has been established. It is, therefore, suitable for abnormal high pressure caused by mudstone under compaction. The most commonly used methods are the acoustic delay method and the interval velocity method.

(1) Acoustic delay method:

$$PP = OBG - (OBG - PP_N)(\frac{DT_N}{DT_O})^x \tag{3-4}$$

(2) Interval velocity method:

$$PP = OBG - (OBG - PP_N)(\frac{V_O}{V_N})^n \tag{3-5}$$

where

PP: Pore pressure, MPa;

OBG: Overburden pressure, MPa;

PP_N: Hydrostatic column pressure, MPa;

DT_N, DT_o: Normal compacted mudstone acoustic delay and acoustic delay of mudstone determined by logging, respectively;

V_N, V_o: Velocities of mudstone formation determined by normal compaction, logging or earthquake, respectively;

n: Eaton index, determined by regional laws or actual drilling data.

In addition, Bowers' method is to determine the vertical effective stress by an

acoustic velocity and empirical parameters, and then subtract the vertical effective stress from the overlying strata pressure to obtain the pore pressure. This method can be used to predict pore pressure caused by unbalanced compaction or other mechanisms.

The prediction of abnormal high pressure caused by unbalanced compaction requires only two empirical parameters. These two empirical parameters can be determined by compaction trend analysis or the adjacent well data.

The abnormal pressure caused by other mechanisms requires more information and additional empirical parameters. In this case, the vertical effective stress in a sediment will be lower than a previous value in the past and in the so-called "unloading" state. It is important to know the historical maximum effective stress value $\sigma_{\max}$ in the sediment. Furthermore, the "unloading" velocity effective stress state of the deposition layer is established and is specified by the unloading parameter U. $\sigma_{\max}$ is calculated from the normal compaction reaction and the user specified value $v_{\max}$. U values are determined by an empirical value, while $v_{\max}$ is the speed when unloading occurs.

$d_{\max v}$ is the "maximum velocity depth", i.e., the depth when unloading occurs, and $depth$ is the total depth.

If unloading does not occur at $d_{\max v} > depth$, then

$$PP = OBG - \frac{\left(\frac{\frac{10^6}{DT} - \frac{10^6}{DT_{ml}}}{A}\right)^{(1/B)}}{depth} \tag{3-6}$$

If unloading occurs at $d_{\max v} \le depth$, then the pore pressure is

$$PP = OBG - \frac{(\sigma_{\max})^{(1-U)}\left(\frac{\frac{10^6}{DT} - \frac{10^6}{DT_{ml}}}{A}\right)^{(U/B)}}{depth} \tag{3-7}$$

and

$$\sigma_{\max} = \left(\frac{\frac{10^6}{DT_{\min}} - \frac{10^6}{DT_{ml}}}{A}\right)^{(1/B)} \tag{3-8}$$

where

DT_{ml} is the corresponding acoustic delay;

A, B, and U are empirical values.

3.2.2.4. 3D pore pressure calculation method

First, an accurate 3D seismic velocity body is obtained by high-precision inversion before or after stacking. Then, based on the prediction of pore pressure in a single well, the 3D pore pressure prediction is realized through either the Eaton or Bowers method with a seismic interval velocity as the constraint condition. The accuracy of the 3D pore pressure prediction depends on the accuracy of the seismic interval velocity. The calculation process is shown in Figure 3.5.

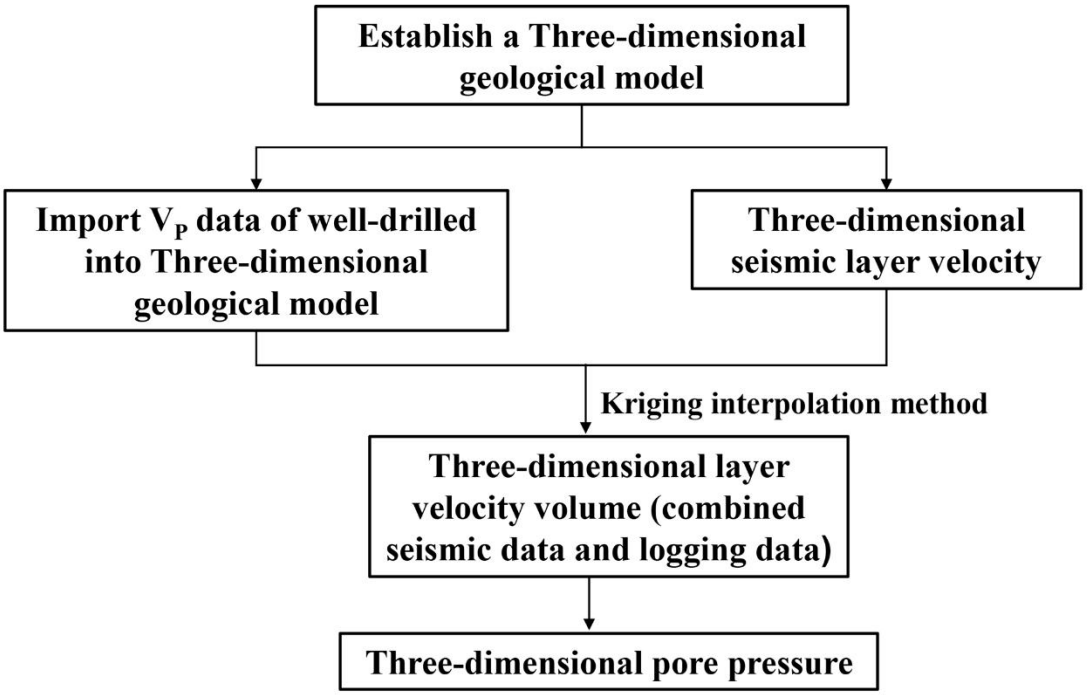

Fig. 3.5 Calculation Method of 3D Pore Pressure

3.2.3. 3D genus model

Attaining an accurate prediction of geomechanical parameters is essential to making accurate predictions about drilling wall stability. At present, the data used to predict geomechanical parameters primarily includes information such as a seismic interval velocity, logging data and measured data with drilling. For mud shale, the geomechanical parameters used to analyze borehole stability mainly include overlying rock pressure, pore pressure, horizontal crustal stress, formation strength parameters, collapse pressure, and rupture pressure.

To calculate the strength parameters of given strata, a series of rock specimens undergo acoustic wave measurements. Using empirical formulas, the results show that a wave velocity in rocks with high compressive strength is also significant. Leveraging Schlumberger's MECHPRO logging method, the mathematical relations

between uniaxial compressive strength and dynamic Young's modulus of sedimentary rocks E_d are established by experiments conducted by Deer and Miller (1966) as follows:

$$UCS = 0.0045 \cdot E_d (1 - V_{cl}) + 0.008 E_d \cdot V_{cl} \quad (3\text{-}9)$$

where

V_{cl} : Mud content of sandstone;

E_d : Dynamic Young's modulus of sandstone, MPa.

The results from a large number of rock mechanical parameters show that the uniaxial compressive strength of rock is generally 8-15 times its tensile strength, so the tensile strength of rock S_t can be calculated by the following formula:

$$S_t = [0.0045 \cdot E_d \cdot (1 - V_{cl}) + 0.008 E_d \cdot V_{vl}] / 12 \quad (3\text{-}10)$$

where

S_t: Tensile strength of rock, MPa.

Coates (1980,1981) presented an empirical relationship between cohesion C and uniaxial compressive strength σ_c of sedimentary rocks:

$$C = A(1 - 2\mu_d)(\frac{1 + \mu_d}{1 - \mu_d})^2 \rho^2 V_p{}^4 (1 + 0.78 V_{cl}) \quad (3\text{-}11)$$

where

A: Constant, depending on the conditions derived from the formula and the unit of calculations used. Under international units, for tertiary mudstone, A is generally 5.44.

Then we calculate the internal friction angle φ by an empirical formula:

$$\varphi = a + b * C \quad (3\text{-}12)$$

$$\rho_b \frac{(3\sigma_H - \sigma_h) - 2CK + \alpha P_p (K^2 - 1)}{(K^2 + 1)H} \times 100 \quad (3\text{-}13)$$

$$K = \tan[(45° + \varphi/2) * 3.14159/180] \quad (3\text{-}14)$$

$$\rho_f = \left[\left(\frac{1 - 2\mu}{1 - \mu} - Q \right) (\sigma_V - \alpha * P_P) + \alpha * P_P + S_t \right] / H \quad (3\text{-}15)$$

where

ρ_b is the collapse pressure gradient, SG;

σ_H is the maximum horizontal in-situ stress, MPa;

σ_h is the minimum horizontal in-situ stresses, MPa;

C is cohesion, MPa;

α is a Biot coefficient;

P_p is the pore pressure, MPa;

H is the depth of a well, m;

φ is the angle of internal friction, degree;

ρ_f is the fracture pressure gradient, SG;

Q is a tectonic stress coefficient;

σ_V is the overburden pressure, MPa;

μ is Poisson's ratio;

S_t is the tensile strength, MPa;

UCS is the compressive strength, MPa;

a, b, A, B, K are the conversion factors.

3.2.4. 3D Crustal Stress Modeling

An underground rock mass is a complex, heterogeneous, anisotropic and nonlinear elastoplastic material. However, the finite element method[54-56] can solve the problem of a stress distribution among heterogeneous, pore and elastoplastic bodies. That is, known crustal stress measurement points (or other reliable methods of crustal stress values) can be put through stress simulations to calculate the whole area of the crustal stress field. This is accomplished, firstly, by gathering the results of a regional geological survey, after which a geomechanical model of the whole study area can be established. By constantly changing the mode and size of boundary forces, the calculated values of tectonic principal stresses (including size and direction) at some specific points in the calculation area can be fitted to the best values of crustal stress at measuring points. The resulting stress-deformation field is the simulation of the present stress-deformation field in the study area.

3.2.4.1. Moore Coulombian elastoplastic guidelines

In this thesis, the Coulomb elastoplastic deformation criterion[57-58] is used to describe the rock deformation state in the study area.

The shear yield surface function of the Moore-Kulun criterion is as follows:

$$F = J - \left(\frac{c}{\tan\varphi} + p \right) \left(\frac{\sin\varphi}{\cos\theta + \sin\theta \sin\varphi / \sqrt{3}} \right) \tag{3-16}$$

$$F = p\sin\varphi + J\left(\cos\theta - \frac{\sin\theta \sin\varphi}{\sqrt{3}} \right) - c\cos\varphi \tag{3-17}$$

where C is the cohesive force, φ is the angle of internal friction, and θ is the stress

Lode angle.

The flow rule Q is given by the same equation, but the internal friction angle φ in the formula is replaced by the shear expansion angle ψ.

Hardening/softening is the cohesive force due to plastic deformation:

$$c = c_0 + HE\varepsilon_{\mathrm{p}}^{\mathrm{d}} \tag{3-18}$$

where c_0 is the initial cohesive force, H is a hardening/softening parameter, E is the elastic modulus, and ε_p^d is the equivalent plastic strain.

$$\varepsilon_{\mathrm{p}}^{\mathrm{d}} = \left[\frac{2\left[\varepsilon_{\mathrm{x}}^2 + \varepsilon_{\mathrm{y}}^2 + \varepsilon_{\mathrm{z}}^2 \right] + \varepsilon_{\mathrm{xy}}^2 + \varepsilon_{\mathrm{yz}}^2 + \varepsilon_{\mathrm{zx}}^2}{3} \right]^{1/2} \tag{3-19}$$

where $\varepsilon_x, \varepsilon_y, \varepsilon_z$ is positive strain while $\varepsilon_{xy}, \varepsilon_{yz}, \varepsilon_{zx}$ is shear strain.

Figure 3.6 shows a relationship between the mohr Coulomb yield and plastic potential functions in a p-J space. F and Q are functions of the stress Lode angle, internal friction angle and shear expansion angle, respectively.

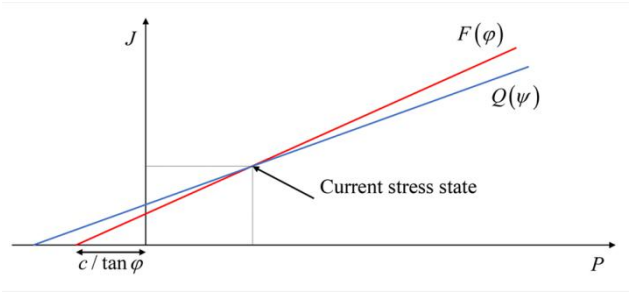

Fig. 3.6 Mohr Coulomb yield and plastic potential functions in *p-J* space

Figure 3.7 shows the yield and plastic potential surfaces on a partial plane.

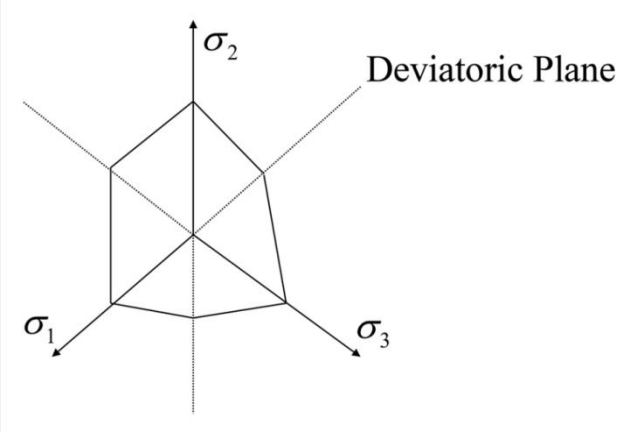

Fig. 3.7 Molar Coulomb yield and plastic potential functions on partial plane

3.2.4.2. Finite element stress field simulation

The finite element method is a numerical technique to solve the problem of a partial differential equation. The domain of interest is locally discretized by small areas of arbitrary shape called finite elements. Therefore, a continuous physical problem is transformed into a discrete finite element problem with unknown node values. A global matrix is obtained by summing the element equations, which are then solved by using numerical linear algebra. Stress and strain are calculated using the joint values and shape functions at the integral (Gaussian) points within each finite element.

The principle of minimum potential energy is used in which: Total Potential energy (E) = Strain energy (W) - work done by applied loads (L). The displacement field with the minimum potential energy can be found. We consider an arbitrary finite element:

$$\delta\Delta E = \delta\Delta W - \delta\Delta L = 0 \tag{3-20}$$

$$\Delta W = \frac{1}{2}\int_{Vol} (\Delta\varepsilon)^T (\Delta\sigma)\, dVol \tag{3-21}$$

$$\Delta L = \int_{Vol} (\Delta d)^T (\Delta F)\, dVol + \int_{Srf} (\Delta d)^T (\Delta T)\, dSrf \tag{3-22}$$

where F is the body strength and T is the boundary traction.

The shape function $[N]$ and node displacement d_i can be used to determine the displacement inside each finite element:

$$(\Delta d) = [N](\Delta d)_i \tag{3-23}$$

Strain can be found from compatibility equations and nodal displacements:

$$(\Delta\varepsilon) = [B](\Delta d)_i \tag{3-24}$$

where $[B]$ is the derivatives of $[N]$.

$$(\Delta\sigma) = [D](\Delta\varepsilon) \tag{3-25}$$

We consider the potential energy in an element. Using constitutive equations eliminates stress:

$$\Delta E = \frac{1}{2}\int_{Vol} (\Delta\varepsilon)^T [D](\Delta\varepsilon)\, dVol - \int_{Vol} (\Delta d)^T (\Delta F)\, dVol - \int_{Srf} (\Delta d)^T (\Delta T)\, dSrf \tag{3-26}$$

Also, by the compatibility equation and shape functions and using node values instead of displacement changes, we have

$$\Delta E = \frac{1}{2}\int_{Vol} (\Delta d)_n^T [B]^T [D][B](\Delta d)_n\, dVol - \int_{Vol} (\Delta d)_n^T [N]^T (\Delta F)\, dVol$$

$$- \int_{Srf} (\Delta d)_n^T [N]^T (\Delta T)\, dSrf \tag{3-27}$$

The minimum potential energy gives the equilibrium equation for each finite element:

$$\delta\Delta E = (\Delta d)_n^T \left[\int_{Vol} [B]^T [D][B](\Delta d)_n\, dVol - \int_{Vol} [N]^T (\Delta F)\, dVol - \int_{Srf} [N]^T (\Delta T)\, dSrf \right] = 0$$

(3-28)

This can be written as:

$$[k_E](\Delta d)_n = (\Delta f_E) \tag{3-29}$$

$$[k_E] = \int_{Vol} [B]^T [D][B] dVol \tag{3-30}$$

$$(\Delta f_E) = \int_{Vol} [N]^T (\Delta F) dVol - \int_{Srf} [N]^T (\Delta T) dSrf \tag{3-31}$$

Each element equilibrium system is assembled into a whole equilibrium system.

In order to solve the general geometry, the elements must be able to adopt a general shape. For this purpose, the elements of a simple shape are used in our systems. Then a relationship is established between the local and global coordinates of each element. The same shape functions for displacement field interpolation are used to specify the relationship between the global coordinate system and the local coordinate system. These elements are then referred to as iso-parametric:

$$(d) = [N](d)_i \tag{3-32}$$

$$(x) = [N](x)_i \tag{3-33}$$

Shape functions [*N*] are specified in local coordinates, as shown in Figure 3.8.

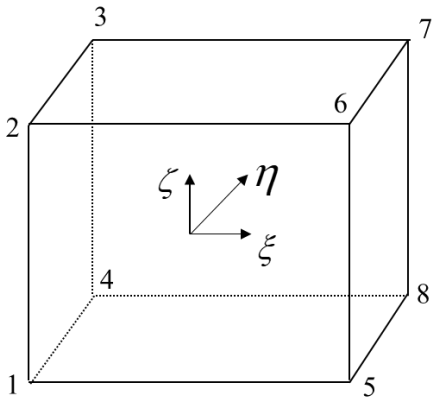

Fig. 3.8 Gauss Point Local Axes

Not only shape functions and also their derivatives in the compatibility matrix [B] are required:

$$[B]=\begin{bmatrix} \partial N_i/\partial x & 0 & 0 \\ 0 & \partial N_i/\partial y & 0 \\ 0 & 0 & \partial N_i/\partial z \\ \partial N_i/\partial y & \partial N_i/\partial x & 0 \\ 0 & \partial N_i/\partial z & \partial N_i/\partial y \\ \partial N_i/\partial z & 0 & \partial N_i/\partial x \end{bmatrix} \tag{3-34}$$

The derivative can be transformed from a local coordinate system to a global coordinate system by the partial differential rule:

$$\begin{pmatrix} \frac{\partial}{\partial \xi} \\ \frac{\partial}{\partial \eta} \\ \frac{\partial}{\partial \zeta} \end{pmatrix} = \begin{bmatrix} \frac{\partial x}{\partial \xi} & \frac{\partial y}{\partial \xi} & \frac{\partial z}{\partial \xi} \\ \frac{\partial x}{\partial \eta} & \frac{\partial y}{\partial \eta} & \frac{\partial z}{\partial \eta} \\ \frac{\partial x}{\partial \zeta} & \frac{\partial y}{\partial \zeta} & \frac{\partial z}{\partial \zeta} \end{bmatrix} \begin{pmatrix} \frac{\partial}{\partial x} \\ \frac{\partial}{\partial y} \\ \frac{\partial}{\partial z} \end{pmatrix} = J \begin{pmatrix} \frac{\partial}{\partial x} \\ \frac{\partial}{\partial y} \\ \frac{\partial}{\partial z} \end{pmatrix} \tag{3-35}$$

where J is the Jacobian determinant. The inverse of J is used to calculate the derivatives in the global coordinate according to the need of matrix [B]:

$$\begin{pmatrix} \frac{\partial}{\partial x} \\ \frac{\partial}{\partial y} \\ \frac{\partial}{\partial z} \end{pmatrix} = J^{-1} \begin{pmatrix} \frac{\partial}{\partial \xi} \\ \frac{\partial}{\partial \eta} \\ \frac{\partial}{\partial \zeta} \end{pmatrix} \tag{3-36}$$

The Jacobian determinant is also used to transform an integral from a global coordinate system to a local coordinate system:

$$\iiint dxdydz = \int_{-1}^{1}\int_{-1}^{1}\int_{-1}^{1} \det|J|\, d\xi d\eta d\zeta \tag{3-37}$$

In the general case of iso-parametric elements, the integrals of the expression of the stiffness matrix and load vector cannot be performed using analytic methods. Instead, the stiffness matrix and load vectors are typically numerically evaluated using Gaussian orthogonality on a quadrilateral region. In the 3D case, the Gauss quadrature formula of a volume integral is:

$$\int_{-1}^{1}\int_{-1}^{1}\int_{-1}^{1} f(\xi,\eta,\zeta)\,d\xi d\eta d\zeta = \sum_{i=1}^{n}\sum_{j=1}^{n}\sum_{k=1}^{n} w_i w_j w_k f(\xi_i,\eta_j,\zeta_k) \qquad (3\text{-}38)$$

where w_i, w_j, w_k are the weighted coefficients, ξ_i, ξ_j, ξ_k are the coordinate positions of each element within the element (abscissa), and n typical values are 1,2 and 3. The evaluation values of stress and strain can also be calculated at these Gaussian points.

3.2.4.3. Boundary condition

The solution of mechanical problems should satisfy the equilibrium, geometric and physical equations. At the same time, a boundary condition should be satisfied on the boundary. Thus, a correct boundary condition is a very important link in mechanical analysis. The simulation of the horizontal stress field is affected by the weight of the overlying strata, pore pressure and tectonic action. Structural stress is mainly realized by applying reasonable boundary conditions, but different boundary conditions will have a significant impact on the calculation results. In this thesis, the strain boundary condition is adopted, and the bottom surface of the model is simply the supported constraint, while the gravity and side boundary displacements are applied simultaneously. By constantly adjusting the lateral boundary displacement,

the crustal stress simulation results can converge to the measured values of crustal stress, as shown in Figure 3.9.

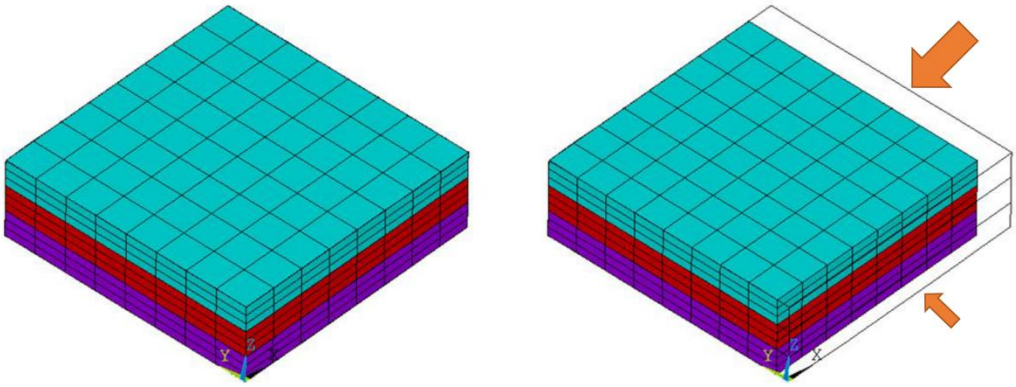

Fig. 3.9 Boundary Load Method

3.3. Chapter summary

This section introduces 3D geomechanical modeling in detail and the working principle in mud shale strata. A 3D geomechanical model with heterogeneity, porosity and elastoplastic is established. The deformation characteristics of shale rock are described by using the Moore Coulomb elastoplastic criterion. As well, both a 3D stress distribution and a 3D safe density window of the shale formation are calculated by the finite element method.

Specific modeling processes include: A. Study area geological model construction; B. Using the Kriging interpolation method and coupling seismic interval velocity data to obtain a 3D interval velocity in the study area, the core algorithm principle of Kriging interpolation method is introduced in detail; C. A series of empirical formulas are used to calculate 3D pore pressure and 3D distributions of

various mechanical parameters; D. Assembly of heterogeneous geomechanical models; E. The deformation state of shale is described by applying the Morkulun elastoplastic criterion; F. The finite element method is used to calculate a 3D stress distribution in mud shale strata, and the core algorithm principle of the finite element method is introduced in detail.

The method provided in this thesis includes the construction and validation of the geomechanical model and simulates the actual 3D stress distribution as far as possible. By using the LOT data provided by the drilled wells, the conditions during the drilling process, the drilling completion data, and the actual drilling conditions of the planned wells in the future, it is possible to continuously validate both the established geomechanical model and the safety density window model. To solve the problem of borehole instability in a mud shale formation, a set of integrated geological-engineering technical schemes is also provided.

CHAPTER IV. 3D Geomechanical Modeling of Indonesia's Oilfield A

4.1. The complexity of drilling and completion in Indonesia's Oil Field A

By the end of 2019, Indonesia's Oilfield A saw a total of nine straight wells and directional wells drilled and completed. The statistics of drilling conditions in the block showed that complex drilling conditions led to a number of issues such as collapse and well leakage and, even more problematically, the borehole itself was scrapped many times, resulting in large economic losses. On average, drilling takes a total of 55 days, while the maximum drilling period is 123 days. Obviously, any time when mud shale collapse leads to borehole instability there is significant downtime in the drilling schedule, and in some cases, side drilling becomes necessary. This puts unnecessary pressure on staff and deprives them of opportunities for other optimizations. For many important reasons, including safety, fast drilling, and an overall reduction in complex accidents, it is suggested that borehole stability management and drilling optimization should be studied carefully.

4.2. Site stress magnitude and direction

4.2.1. Leak off test (LOT)

A leak off test is conducted by injecting a small flow of a high-pressure fluid into the test section (the flow rate is generally less than 100L/min) until the formation ruptures and the pump is stopped. Then multiple fracture extension and closure tests

are conducted to obtain reliable and repeatable fracture closure pressures (LOT), resulting in the horizontal minimum principal stress (LOT value). Part of the drilled well in this block has carried out ground breaking experiments. Thus, a small amount of LOT data is already obtained (Figure 4.1).

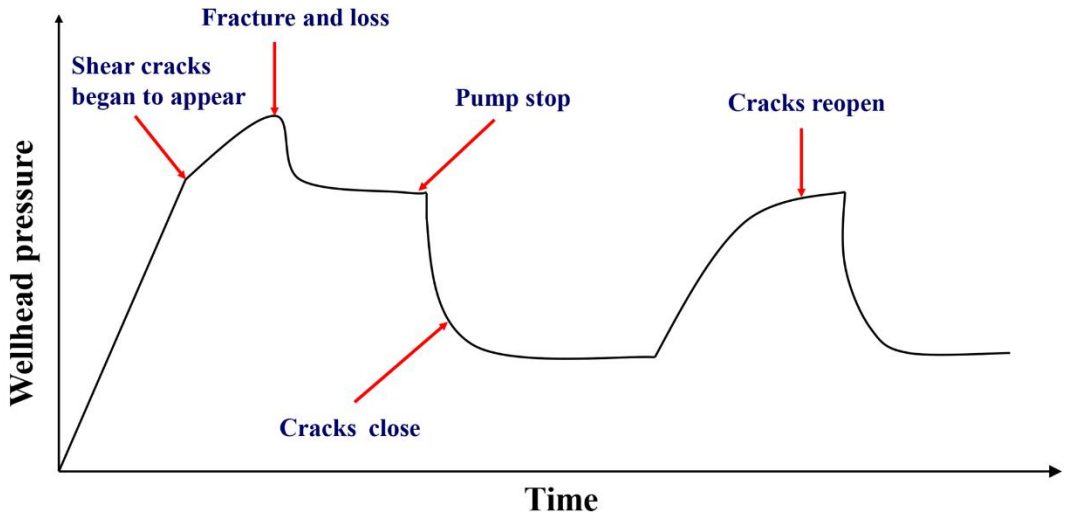

Fig. 4.1 Hydraulic fracturing test curve

4.2.2. Direction of minimum crustal stress

The azimuth of the borehole rupture comes from the FMI diagram of Well A-4. The borehole rupture can be identified in the vertical direction near a depth of 1417m to 1383m. The minimum horizontal stress direction is about 110±5°NW-SE, as shown in Figure 4.2.

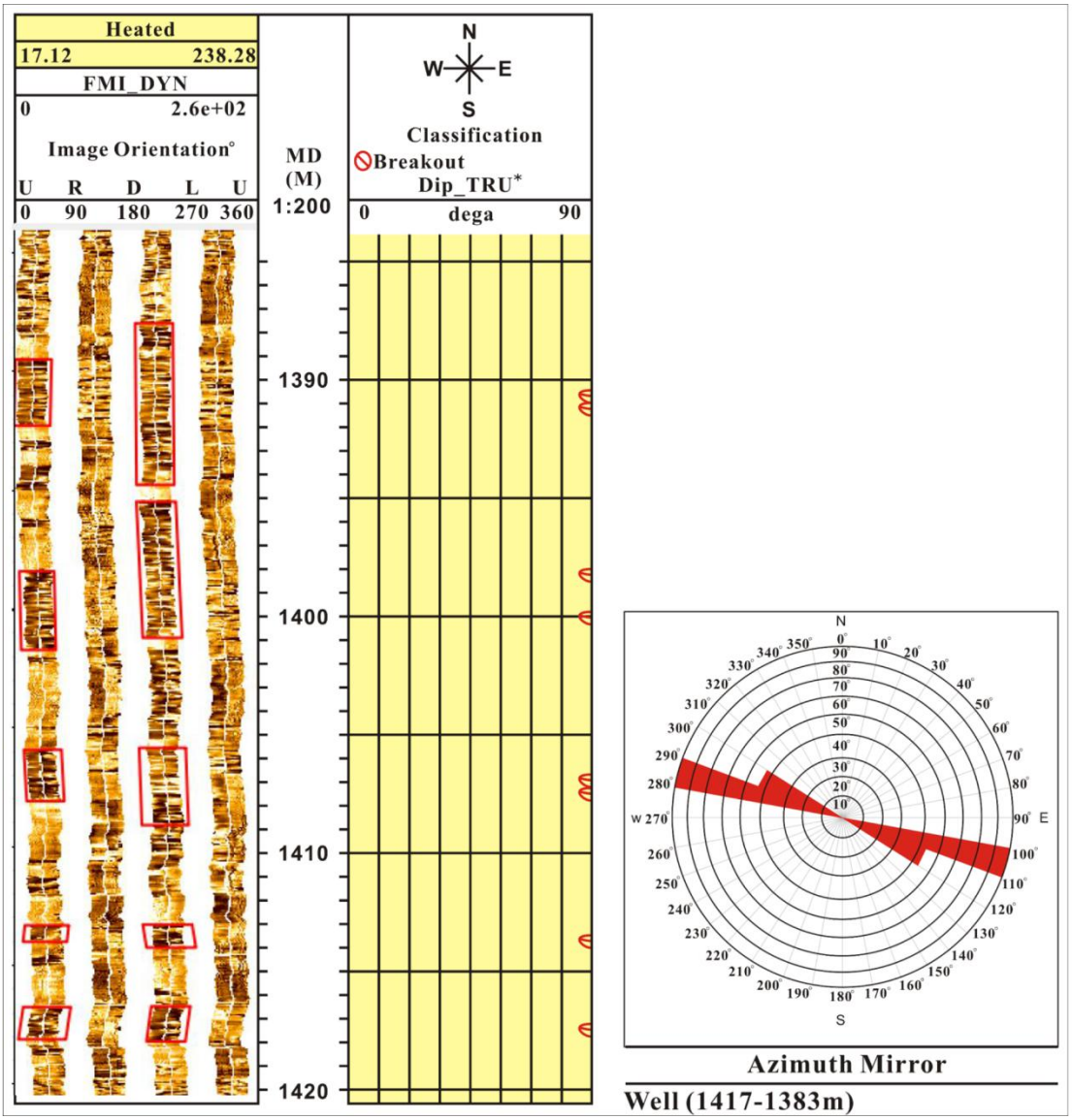

Fig. 4.2 Minimum stress direction

4.3. Geomechanical modeling of Oilfield A

The physical, chemical, and mechanical characteristics of mud shale in Indonesia's Oilfield A need to be clarified, and are used to calibrate the 3D geomechanical modeling results in Chapter III. To facilitate this discussion, Chapter II of this these has carried out a detailed experimental study on the various properties of shale in the different strata of Oilfield A.

4.3.1. 3D geomechanical model

Using the Petrel software platform's geomechanical module, a geomechanical grid of Indonesia's Oilfield A is generated. As shown in Figures 4.3 and 4.4, the modeling area of the A block in Indonesia is 77km^2. The *Z* direction of the workspace is 0m to 28448m. But the formation grid below 3100m is sparsely treated, focusing primarily on the vertical region of 0-2500m. The distribution of strata from top to bottom is as follows: the Cisubuh formation, Parigi formation, Cibulakan Atas formation and finally, the MMC formation. The total number of finite elements is 1,576,810. Obviously, this is a huge model that requires a lot of human input and support from computer hardware.

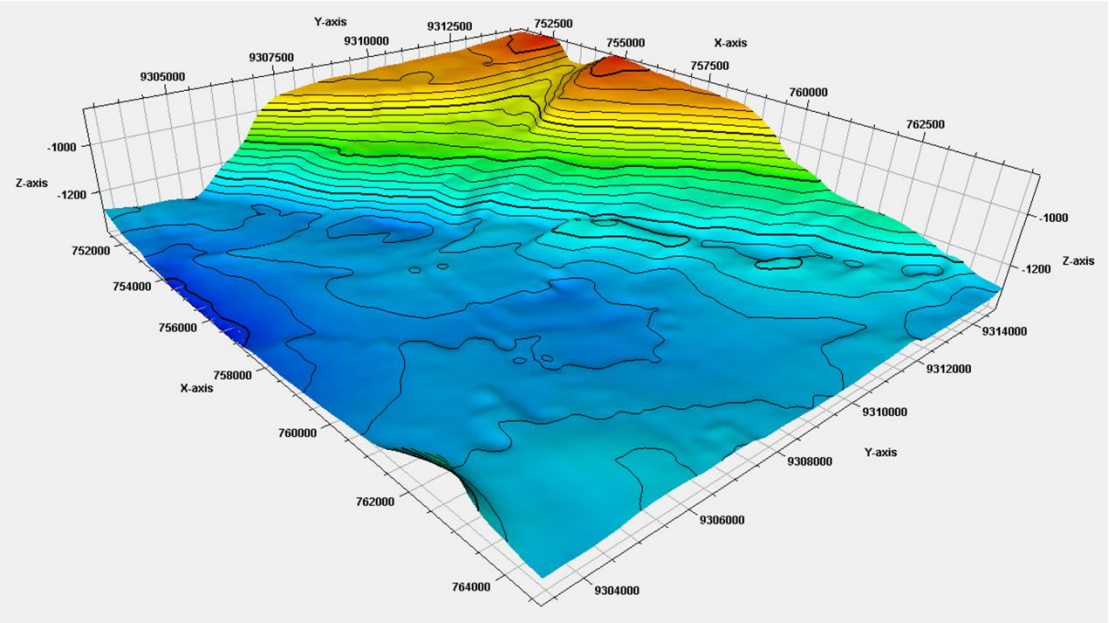

Fig. 4.3. Indonesia Oilfield A work area

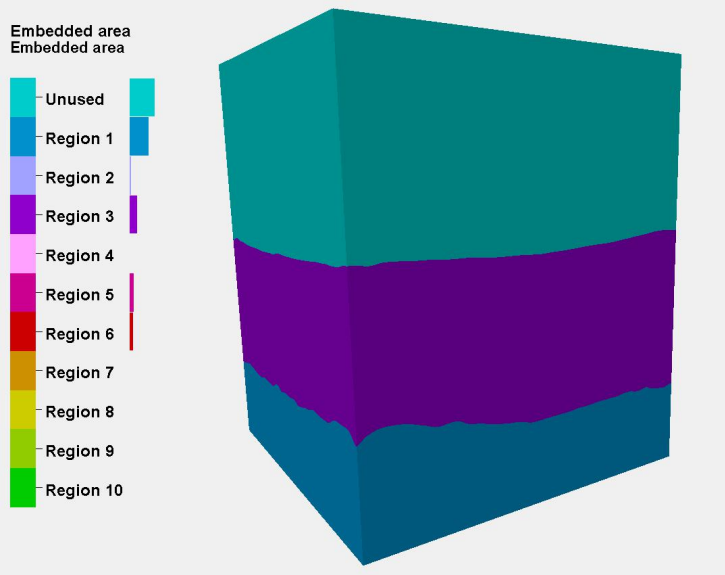

Fig. 4.4 3D geological model of Indonesia Oilfield A

4.3.2. 3D pore pressure of Indonesia Oilfield A

4.3.2.1. Pressure mechanism analysis

Based on engineering analysis, the pressure formation mechanism of shale in Oilfield A is then predicted. The intersections of the acoustic delay density of wells A-4 and A-9 at the Cisubuh and Cibulakan Atas formations are drawn, respectively. Well A-9 is under compacted at the Cibusuh formation as shown in Figure 4.5, while Well A-4 is shown to be in a normal compaction state. Therefore, it can be assumed that abnormal pressure of under compaction may be present in some blocks of the Cisubuh formation in Oilfield A. Accordingly, this thesis uses the Eaton formula to estimate pore pressure in Oilfield A. This also coincides with instances of serious collapse experienced in this well section during drilling. Generally, the higher the pore pressure, the higher the collapse pressure.

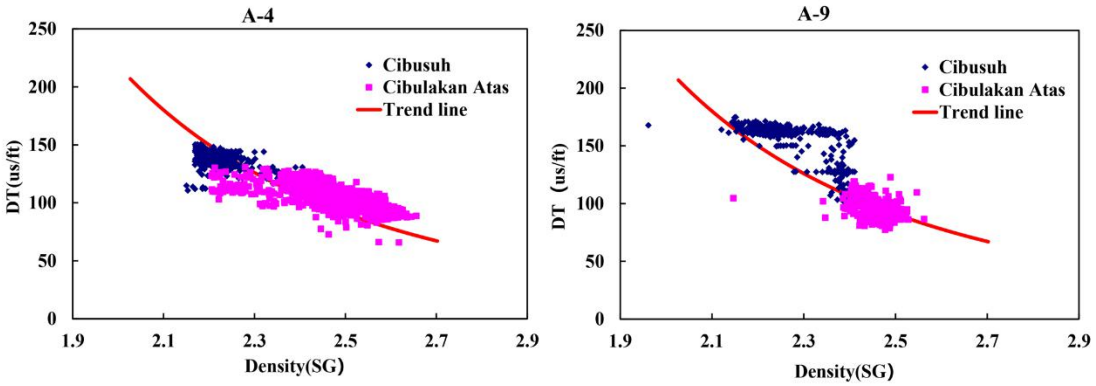

Fig. 4.5 Density and acoustic delay intersections of wells A-4 and A-9

4.3.3.2. 3D pore pressure results

Figure 4.6 shows the results of intermediate variables and 3D pore pressure in the overall calculations of 3D pore pressure. The 3D geological model of Oilfield A includes the Cisubuh, Parigi, Cibulakan Atas and MMC formations. The 3D seismic interval velocity is obtained by inverting the seismic wave data, ranging from 1752m/s to 6584m/s. The 3D interval velocity is interpolated by the Kriging interpolation method, which combines both the drilled interval and the seismic interval velocities. The numerical range is 1648m/s to 6130m/s. The results show that the seismic interval velocity is consistent with the 3D interval velocity of Oilfield A in different strata, but the 3D interval velocity is more precise. The 3D visualization of the pore pressure distribution in Oilfield A is then calculated. The 3D pore pressure is 0MPa to 56.72MPa, and the 3D pore pressure gradient is 0.97SG to 1.23SG. Where the Cisubuh and Parigi formations have high pressure zones, the figure shows yellow and red, and the maximum pore pressure is up to 1.23G. The Cibulakan Atas and MMC formations contain normal pressure gradients.

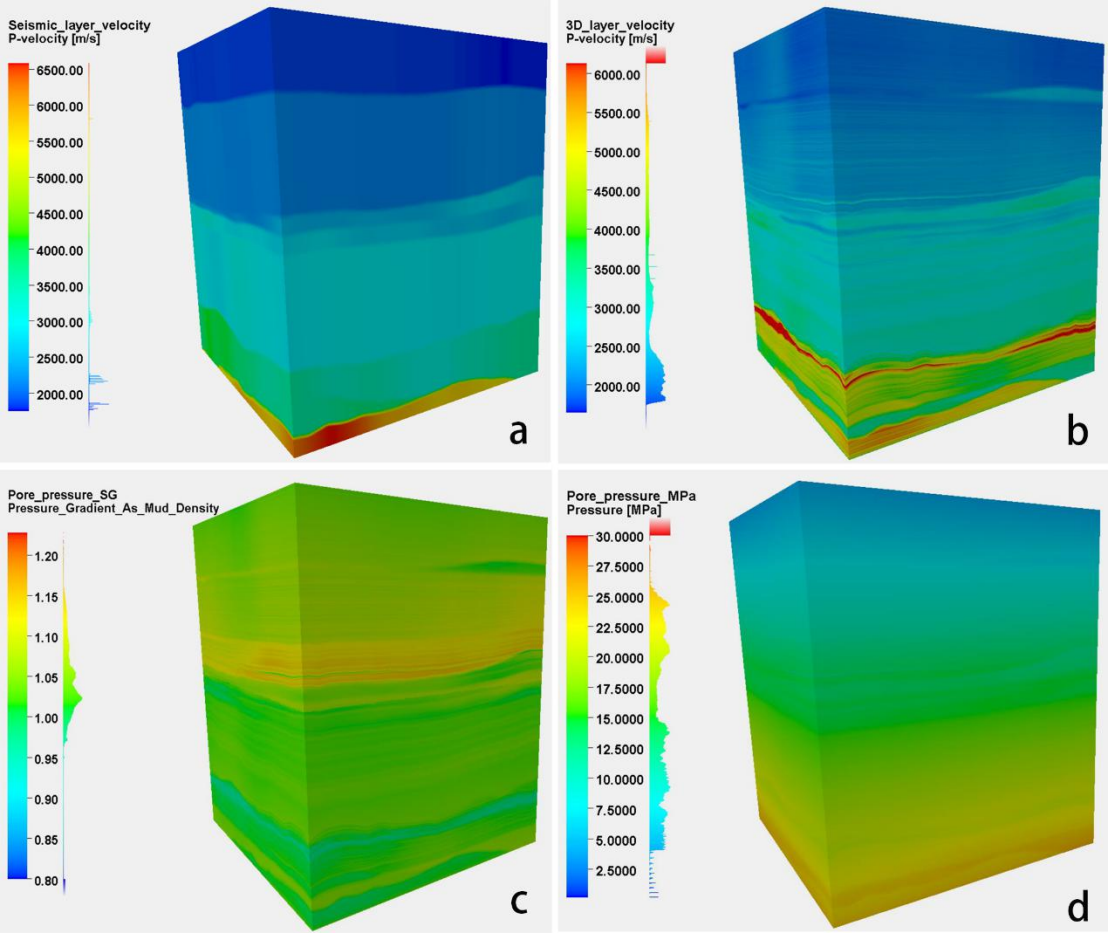

Fig. 4.6 Calculation procedure and results of 3D pore pressure

The figures above demonstrate instances where: (a) the 3D seismic interval velocity ranges from 1752m/s to 6584m/s; (b) the 3D interval velocity ranges from 1648m/s to 6130m/s; (c) the 3D pore pressure gradient ranges from 0.97SG to 1.23SG; and (d) the 3D pore pressure ranges from 0MPa to 56.72MPa.

4.3.3. Results of 3D Genuine

Through a combination of logging data, laboratory lithology test results and a series of empirical formulas, mechanical parameters such as Young's modulus, Poisson's ratio, the compressive strength, tensile strength, cohesion and internal friction angle of Oilfield A are calculated. The results are shown in Figure 4.7.

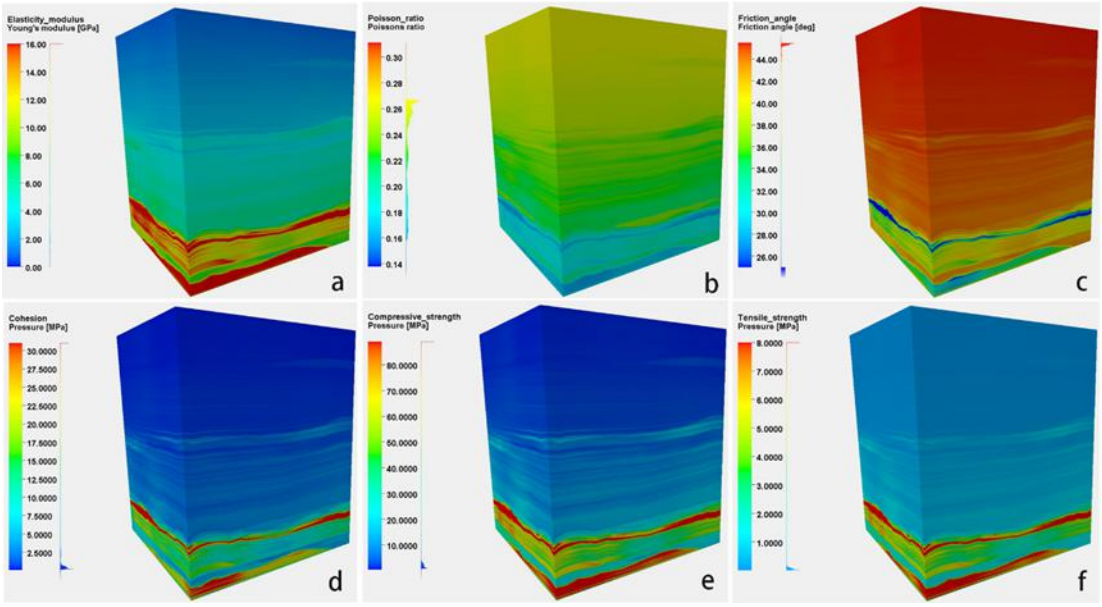

Fig .4.7 3D genus distribution of Indonesia Oilfield A

These graphs show where: (a) the 3D Young's modulus ranges from 0.64GPa to 15.30GPa; (b) the 3D Poisson's ratio ranges from 0.18 to 0.28; (c) the 3D internal friction angle ranges from 33.81° to 45.49°; (d) the 3D cohesion ranges from 0.10MPa to 30.69MPa; (e) the 3D compressive strength ranges from 0.50MPa to 88.75MPa; and finally, (f) the 3D tensile strength ranges from 0.02MPa to 7.91MPa.

4.3.4. Calculations of 3D crustal stress

The crustal stress distribution of Oilfield A is calculated using the finite element method based on the Petrel software platform's geomechanical module. Figure 4.8 shows the final calculation results of the 3D maximum horizontal stress, the 3D minimum horizontal stress and the 3D vertical stress. Based on these results, it can be seen that the maximum horizontal stress ranges from 6.90MPa to 49.17MPa. The minimum horizontal stress ranges from 6.17Mpa to 43.33MPa. Finally, the overburden pressure ranges from 7.38MPa to 54.88MPa. Overall, overburden

pressure >max horizontal stress >min horizontal stress, which indicates that Indonesia's Oilfield A belongs to the control range of positive faults.

The calculated results of the minimum crustal stress present in Oilfield A are calibrated using the LOT data of the drilled oil field. The results are shown in Table 4.1. It is found that the LOT value and minimum crustal stress calculations have relatively small errors, and the maximum relative error is only 0.02. However, due to the relatively limited amount of data used for these calibrations, the model must be continuously validated and optimized in future drilling and completion processes.

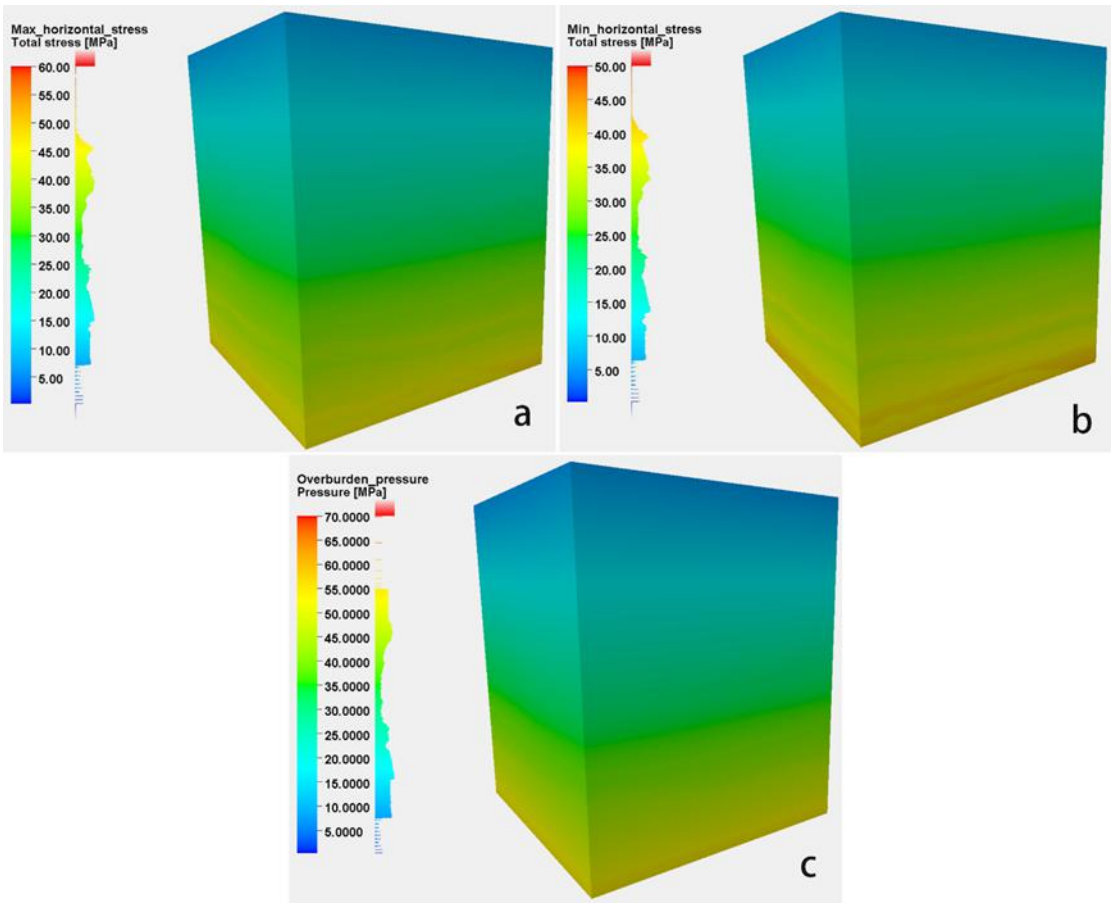

Fig. 4.8 Calculation of 3D crustal stress

The figures presented above demonstrate where: (a) the maximum horizontal stress

ranges from 6.90MPa to 49.17MPa; (b) the minimum horizontal stress ranges from 6.17MPa to 43.33MPa; and (c) the overburden pressure ranges from 7.38MPa to 54.88MPa.

Table 4.1 Calibration of Minimum Crustal Stress Calculation Model

Well	Well-type	Measured Depth m	Total Vertical Depth m	LOT SG	LOT MPa	Min horizontal stress Mpa	Relative error %
A-2	vertical well	1274	1274	1.68	21.00	20.42	0.02
A-4	directional well	1383	1383	1.70	23.06	22.84	0.02
A-7	directional well	1625	1500	1.68	24.72	24.54	0.01
A-8	directional well	1730	1633	1.71	27.39	27.45	0.01
A-9	directional well	1425	1105	1.74	18.86	18.52	0.01

4.3.5. Security Density Window Results

An important step in geomechanical modeling is to determine the optimal mud pressure for safe drilling through a calculated 3D crustal stress model. Whether the calculated density window is credible or not also indirectly verifies whether the calculation model of crustal stress is reliable. Successful design of mud pressure should effectively avoid borehole rupture or borehole instability during drilling. As such, the collapse pressure and rupture pressure are calculated by the empirical formula listed in Section 2.5.5. The results are shown in Figure 4.9. In general, the collapse pressure gradient ranges from 0.6SG to 1.47SG. However, the Cisubuh formation collapse pressure is a bit high, up to 1.47SG. The MMC reservoir formation

is stable although there is still some collapse risk due to shale development in some well sections. The fracture pressure gradient ranges from 1.71SG to 2.02SG. In addition, the calculated security density window can be viewed in 3D. For any planned well location in the working area, the corresponding security density window can be quickly given as long as the coordinate position is established. Thus, it can intuitively and efficiently guide drilling and completion in the work areas of Oilfield A.

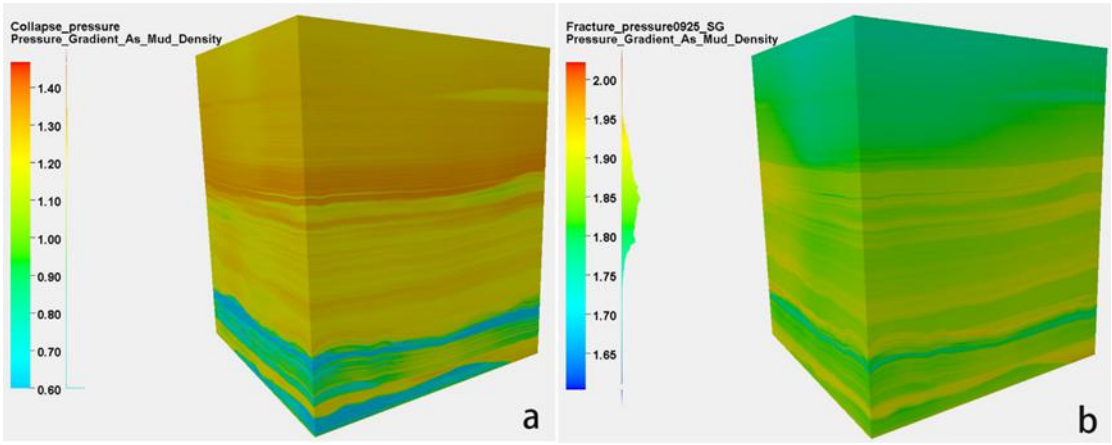

Fig. 4.9 Calculation results of 3D security density window.

The graphs above illustrate where: (a) the collapse pressure gradient ranges from 0.6SG to 1.47SG and (b) the fracture pressure gradient ranges from 1.71MPa to 2.02MPa.

4.4. Field Application

Well A-10 is a developed directional well, with a maximum well deviation of 20.28°, and the target formation is the MMC reservoir stratum. Based on the calculated 3D crustal stress and 3D safety density window, the drilling design of Well A-10 is optimized. As such, Well A-10 adopts a four-section structure. Data from Well

A-10 was extracted from the 3D density window model, as shown in Figure 4.10.

In terms of actual drilling, the first section used 26-inch drill bits to 349m, while the second section used 17.5-inch drill bits to 1474m, thereby drilling through the Parigi formation. The collapse pressure calculated by the model was 1.24SG to 1.35SG, the rupture pressure was 1.78SG to 2.00SG, and the pore pressure was up to 1.23SG. The drilling fluid density was calculated at 1.35SG to 1.56SG. In summary, the drilling process was smooth. The background gas was 1-50 and 80-120 units, and the gas reached its total peak content at 200-370 units in the shale's sandstone layers. The pore pressure of this section was monitored in real time through the mechanical specific energy method (Majidi et al.,2017), and the calculated results showed up to 1.33SG. Interestingly, the pore pressure calculated by the mechanical specific energy method was larger than the pore pressure data provided by the 3D model of Oilfield A. However, the results of both calculations showed that there was high pressure in the middle and lower formations of the Cisubuh and Parigi.

The third section used 12.25-inch drill bit to 1973m, reaching the top of the MMC reservoir formation. The collapse pressure was 0.80SG to 1.35SG, and the rupture pressure was 1.90SG to 2.02SG. The pore pressure was found to be at a normal pressure gradient, and the drilling fluid density was 1.40SG to 1.41SG. This section was also drilled smoothly. The background gas was from 15-30 units and 60-100 units, while the total gas content peaked at 200-520 units in the sandstone formation.

The fourth and final section used an 8-inch drill bit to open the MMC reservoir,

at which point the drilling continued to the borehole bottom, finished at a drilling depth of 2084m. The collapse pressure calculated by the model was 0.80SG to 1.24SG, and the rupture pressure was 1.89SG to 1.91SG. Pore pressure was found to be at a normal pressure gradient, and the drilling fluid density was 1.10SG. The calculated values of collapse pressure in some of the well sections were large and were likely developed mud shale. In all, the drilling process was smooth. The background gas was 20-60 units, and the total gas content peaked at 100-800 units in the sandstone layers.

From the actual drilling data gathered from well A-10, the collapse pressure and rupture pressure calculated by the 3D model have been verified. At the same time, there is a direct correspondence between the maximum crustal stress, the minimum crustal stress and the collapse pressure, so the 3D safe density window calculation model is also used to constrain the minimum crustal stress and the maximum crustal stress calculation model. Well A-10 was drilled on October 6th, 2020 and completed on November 2nd, 2020. The drilling cycle was 28 days, compared to an average 55-day drilling period in the remainder of Oilfield A. The drilling cycle was shortened by 49% and there were no complex accidents in the drilling process. In summary, the established 3D pore pressure, collapse pressure, rupture pressure, crustal stress and other models were verified. A confident geomechanical model and density window model have finally been determined.

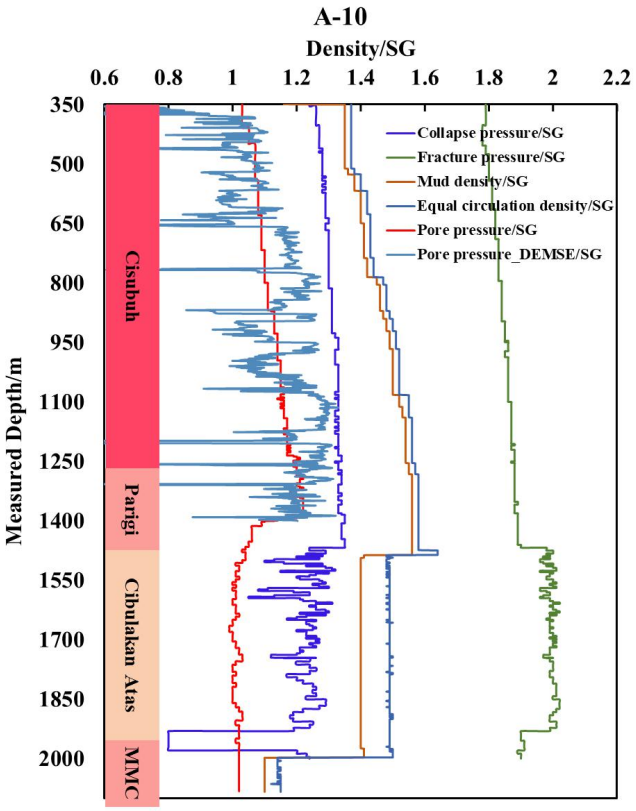

Fig. 4.10 A-10 Safe Drilling Density Window

4.5. Chapter Summary

1. Based on a series of core tests, well logging data and seismic inversion data, the mechanical parameters of Oilfield A in Indonesia have been described in detail. The 3D heterogeneous mechanical parameter distribution and 3D pore pressure distribution of Oilfield A have been established. In total, the 3D pore pressure ranged from 0MPa to 56.72MPa, while the 3D pore pressure gradient ranged from 0.97SG to 1.23SG. Where the Cisubuh and Parigi formations have been shown to possess high pressure zones, the Cibulakan Atas and MMC formations have normal pressure gradients.

2. Using the finite element method, the 3D stress distribution has been obtained

by using the heterogeneous pore elastic-plastic model. The results show that the maximum horizontal stress ranges from 6.90MPa to 49.17MPa, and the minimum horizontal stress ranges from 6.17MPa to 43.33MPa. Overburden pressure, on the other hand, ranges from 7.38MPa to 54.88MPa. Overall, overburden pressure > max horizontal stress > min horizontal stress, and Indonesia's Oilfield A belongs to the control range of positive faults.

3. The results of the minimum crustal stress calculations of Oilfield A have been calibrated using LOT data from the drilled oil field. The LOT value and minimum crustal stress calculation results have shown relatively few errors, and the maximum relative error is only 0.02. The minimum horizontal stress direction is about 110±5°NW-SE.

4. 3D collapse pressure and 3D rupture pressure have been calculated by the empirical formula. The calculated 3D safety density window has been visualized, and the collapse pressure gradient has been shown to range from 0.6SG to 1.47SG. The results show that the Cisubuh formation has the highest collapse pressure of up to 1.47SG. While the MMC reservoir formation is relatively stable, there is still some collapse risk due to shale development in other well sections. The fracture pressure gradient has been shown to range from 1.71MPa to 2.02MPa.

5. From planned well A-10’s actual drilling data, both the collapse and rupture pressure calculated by the 3D model have been verified. Therefore, both a confident geomechanical model and a density window model have finally been determined.

CHAPTER V. CONCLUSIONS AND FUTURE WORK

A detailed study on the physical, chemical and mechanical properties of mud shale in Indonesia's Oilfield A was carried out through laboratory mineral analysis, electron microscopy, cation exchange capacity and the parameters of rock mechanics. Experimental results were the cornerstone of the eventual 3D geomechanical modeling performed for Oilfield A. Based on the Petrel software platform, a set of 3D geomechanical modeling methods and principles of shale were introduced in detail. A complete 3D geomechanical model was, therefore, produced, which was successfully applied in field drilling. The main conclusions of this thesis are as follows:

(1). According to the physical and chemical characteristics of the mud shale formation in Indonesia's Oilfield A, the collapse risk of shale in the different strata was obtained.

The experimental samples were taken from the Cisubuh, Parigi and Cibulakan Atas formations of Oilfield A. The content of clay found in these three formations was not considered high; however, all three formations contained montmorillonite, which indicated that these formations all have strong water absorption and expansion characteristics.

The mud shale found in Oilfield A is relatively dense, but there are fractures in grains, which have a width of about 5-10 μm. Some samples were filled with calcite and layered or flaky mixtures of illite-montmorillonite. The layered structure and intergranular pore joints of these minerals were shown to increase drilling fluid seepage and, therefore, lead to adverse effects on wellbore stability. Mud shale from

the Cisubuh formation was shown to have a certain ability to absorb and expand. If exposed to drilling mud over a long period of time, boreholes in this formation are more likely to collapse. The Cibulakan atas formation, on the other hand, belongs to hard mud shale with moderate dispersion and spalling trends. Because of its hard brittleness, micro fractures are relatively well-developed in this formation.

(2). Through studying the mechanical characteristics of mud shale in the Cisubuh formation, the mud shale's mechanical parameters were obtained. The experimental results were then used to produce 3D geomechanical modeling and calibrations.

The experimental results showed that the uniaxial compressive strength of the core sample was between 6-35MPa. Under confining pressure, the core compressive strength increases. In total, the compressive strength was above 40MPa under 10-30MPa confining pressure. In addition, the elastic modulus was about 2-10GPa under uniaxial conditions, and Poisson's ratio was about 0.20-0.27. According to the Mohr-Coulomb criterion, the cohesive force of shale is between 2MPa to 9MPa. Additionally, the internal friction angle is approximately 41°, and the ability to resist shear failure is poor. Overall, the tensile strength is between 0.5-3MPa. Compared with the uniaxial compressive strength data, it is found that the uniaxial compressive strength is about 12 times that of the tensile strength.

The failure modes of mud shale are primarily due to splitting failures and single shear failures. Under uniaxial compression, splitting failure occurs most consistently, and single shear failure occurs mainly under triaxial compression. The rock shows strong brittleness. In addition, with an increase in confining pressure, the failure

strength of the test core increases, and the deformation characteristics of the rock show a transition from brittleness to plasticity under low confining pressure.

(3). Through the introduction of 3D geomechanical modeling and principles of the shale formation, the scientific nature and effectiveness of 3D geomechanical modeling of shale have been expounded.

3D geomechanical modeling and working principles of the mud shale formation were introduced in detail by establishing heterogeneity and porosity. The elastoplastic 3D geomechanical model, therefore, completes the calculations of the 3D stress distribution and the 3D safe density window of the shale strata under study.

(4). A complete 3D geomechanical model of Indonesia's Oilfield A was obtained through 3D crustal stress distribution and the 3D security density window.

Through a series of core tests, well logging data, seismic inversion data, the mechanical parameters of Indonesia's Oilfield A were described in detail. As a result, the 3D heterogeneous mechanical parameter distribution and 3D pore pressure distribution were established. The 3D pore pressure was found to range from 0MPa to 56.72MPa, and the 3D pore pressure gradient was found to range from 0.97SG to 1.23SG. Where the Cisubuh and Parigi formations have high pressure zones, the Cibulakan Atas and MMC formations possess normal pressure gradients.

Using the finite element method, the 3D stress distribution was obtained using the heterogeneous pore elastic-plastic model. As a result, it was shown that the max horizontal stress ranged from 6.90MPa to 49.17MPa, while the min horizontal stress ranged from 6.17MPa to 43.33MPa. The overburden pressure ranged from 7.38MPa

to 54.88MPa. Overall, overburden pressure>max horizontal stress >min horizontal stress, and it was determined that Oilfield A belonged to the control range of positive faults.

Both the 3D collapse and 3D rupture pressures of Oilfield A were calculated by empirical formulas. Furthermore, the 3D safety density window was visualized. As a result, it was shown that the collapse pressure gradient ranged from 0.6SG to 1.47SG. The Cisubuh formation was shown to have the highest collapse pressure, up to 1.47SG. Meanwhile, it was determined that the MMC reservoir formation was stable although there remains some collapse risk due to shale development in certain well sections. The fracture pressure gradient was shown to range from 1.71MPa to 2.02MPa.

(5). Comprehensive analysis of wellbore stability and technical countermeasures for planned well A-10 in was provided.

Engineering preparation before drilling: Based on the calculated values for 3D crustal stress and the 3D safety density window, the drilling design of well A-10 was optimized. Indeed, the design took into account the fact that both the Cisubuh and Parigi formations' mud shale collapse pressure was high, while the mud shale collapse pressure in the Cibulakan Atas formation was slightly lower. By designing different casing structures, the Cisubuh, Parigi and Cibulakan Atas strata were separated. As a result, well A-10 underwent a four-section structure.

Real-time tracking and drilling management optimization: During drilling, pore pressure in the Cisubuh and Parigi formations was monitored in real time by a

mechanical specific energy method. The calculated results were up to 1.33SG. The pore pressure calculated by the mechanical specific energy method was larger than the pressure provided by the 3D model of Oilfield A. However, the results of both calculations show that there is high pressure in the middle lower sections of both the Cisubuh and Parigi formations.

(6). Model calibration.

The calculated results of the minimum crustal stress present in Oilfield A were calibrated using the LOT data from the drilled oil field. Both the LOT value and minimum crustal stress calculations showed relatively few errors, and the maximum relative error was only 0.02. The minimum horizontal stress direction was about 110±5°NW-SE.

Compared to an average drilling period of 55 days in Oilfield A, Well A-10's drilling cycle was 28 days, thereby shortening the drilling cycle by 49%. There were no records of complex accidents throughout the drilling process. In this way, the established 3D pore pressure, collapse pressure, rupture pressure, crustal stress and other models were verified. A confident geomechanical model and a density window model were finally determined.

In summary, the modeling method provided in this thesis makes full use of core tests, drilled logging data, and seismic inversion data. A complete construction and verification of the geomechanical model was provided, and a simulation of the 3D stress distribution law of mud shale formations was shown as accurately as possible. By using LOT data from drilling, accounting for complex conditions during the

drilling process, the drilling completion data, and the actual drilling conditions of planned wells in the future, the established geomechanical model and safety density window model have been continuously verified. Therefore, in order to solve the problem of wellbore instability in mud shale formations, a set of integrated geological engineering techniques have been provided.

All the experimental, modeling and simulation studies in this thesis have been applied to Indonesia's Oilfield A. The future work will be to extend them to other oil and gas fields in the world.

References

[1] Chen M., Jin Y. Advances and Developmental Trend of the Wall Stability Technique. Petroleum Drilling Techniques, 2005, 33(5): 28-34.

[2] F.J.Santarelli, Stefano Carminati. Do shales swell? A Critical Review of Available Evidence. SPE/IADC 29421, 1995.

[3] Wang J.H., Yan J.N., Shu S.N. New method for evaluating borehole stability in brittle shale. Petroleum Drilling Techniques, 2006, 28(2): 28-30.

[4] Horacio Fontana, Martín Paris, Seehong Ong. Borehole Stability (Geomechanics) Modeling and Drilling Optimization Practices Improve Drilling Curves in Naturally Fractured Shale-A South Argentina Experience. SPE/IADC 107474, 2007.

[5] Liu R.S., Zeng Y.J. Technical difficulties and countermeasures of drilling under complex conditions. Beijing: China Petrochemical Press, 2005, 9.

[6] Yu B.H., Deng J.J., Yan W. Borehole Sloughing Control in Shale Formations. Petroleum Drilling Techniques, 2010, 38(1): 56-59.

[7] Xiao K., Zhou C.C., Huang Z.H. Study on logging response characteristics and identification method of shale gas reservoir. Science & Technology Review, 2012, 30(18): 73-79.

[8] Liu X. Chen B., &Wu C.L. Drilling technique of Well BY-1HF for shale reservoir. Petroleum Drilling Techniques, 2012, 34(4): 5-11.

[9] Jiang Z.H., Tong S.B., Ding J.H. Key Technologies Adopted for Shale Gas Horizontal Well PengyeHF-1. Petroleum Drilling Techniques, 2012, 40(4): 28-31.

[10] Wang H.P., Zhang D., &Yu J.Q. Drilling Technologies on Shale Gas in Weiyuan Structure. Drilling & Production Technology, 2012, 35(2): 9-11.

[11] Wang J.L., Hei G.X., Zhao H.X. Drilling & Completion Techniques Used in Shale Gas Horizontal Well YSH1-1 in Zhaotong Block. Petroleum Drilling Techniques, 2012, 40(4): 23-27.

[12] Liang X., Wang G.C., Zhang J.H., &Li Z.F. High-efficiency integrated shale gas development model of Zhaotong National Demonstration Zone and its practical enlightenment. China Petroleum Exploration, 2017,22(1):29-37.

[13] Xie J., Zhang H.M., She C.Y., &Yang Y. Practice of geology-engineering integration in Changning State Shale Gas Demonstration Area. China Petroleum Exploration, 2017,22(1):21-28.

[14] Zhang Y., Yang X.T., Teng Q., &Xu G. Peng Fen. Practice and cognition of

geology-engineering integration for the production increasing of HTHP ultra-deep tight gas reservoir in Tarim oilfield. China Petroleum Exploration, 2018,23(2):43-50.

[15] Liu N.Z., Wang G.Y., Xiong X.L. Practice and prospect of geology-engineering integration technology in the efficient development of shale gas in Weiyuan block. China Petroleum Exploration, 2018,23(2):59-68.

[16] Wu Q., Liang X., & Li X. Geoscience-to-production integration ensures effective and efficient South China marine shale gas development. China Petroleum Exploration, 2015,20(4):1-23.

[17] Zhang H., Yi S.D., Bernt S.A. Poroelastic modeling of borehole breakouts for crustal stress determination by finite element method. Journal of Petroleum Science and Engineering, 2018, 162: 674-684.

[18] Hayashi, M., Kanagawa, T., Hibino, S., Motozima, M., Kitahara, Y. Detection of anisotropic geo-stresses trying by acoustic emission, and non-linear rock mechanics on large excavating caverns. Proceedings of the 4th ISRM Congress. Montreux, Switzerland: International Society for Rock Mechanics and Rock Engineering. 1979, 211-218.

[19] Teufel, L. W. crustal stress and natural fracture distribution at depth in the Piceance Basin, Colorado: implications to stimulation and production of low permeability gas reservoirs. In The 27th US Symposium on Rock Mechanics (USRMS). American Rock Mechanics Association. 1986, January.

[20] Wang, H., Wang, W., Wang, L., Sun, B. S., & Xia, B. R. Three dimensional tectonic stress field and migration of oil and gas in Tanhai. Acta Geoscientia Sinica, 2002, 23(2; ISSU 68), 175-178.

[21] Zoback, M.D. Reservoir Geomechanics. Cambridge University Press. 2007.

[22] Y. Wileveau, F. H. Cornet, J. Desroches, P. Blumling. Complete crustal stress determination in an argillite sedimentary formation. Physics and Chemistry of the Earth, 2007, 32(8), 866-878.

[23] Meng Z.P., Zhang Ji.C., Wang R. crustal stress, pore pressure and stress-dependent permeability in the Southern Qinshui Basin. International Journal of Rock Mechanics and Mining Sciences, 2011, 48(1), 122-131.

[24] Yin, S., Zhang, J. & Liu, D. A study of mine water inrushes by measurements of crustal stress and rock failures. Nat Hazards 79, 1961–1979 (2015). https://doi.org/10.1007/s11069-015-1941-1.

[25] Xiao H.T., Xu H.Y. In situ permeability measurements to establish the influence of slice mining on floor rocks. Int J Rock Mech Min Sci, 2000(37):855–860.

[26] Wu, Z., Chen, Q. , Barosh, P. , Peng, H. and Hu, D. Stress rise precursor to earthquakes in the Tibetan Plateau. Natural Science, 2013, 5, 46-55. doi: 10.4236/ns.2013.58A1006.

[27] Li, F.Q. crustal stress measurement is an important approach to realize earthquake prediction—Developing J.S. Lee's scientific ideas on earthquake prediction. In: Xue and Furen, Eds., Rock Stress and Earthquakes, CRC Press, Taylor and Francis Group, London, 2010, 757-759.

[28] Wu, M.L., Zhang, C.S., Liao, C.T., Ma, Y.S. and Ou, M.Y. The recent state of stress in the central Qinghai-Tibet Plateau according to crustal stress measurements. Chinese Journal of Geophysics, 2005, 48, 327-332.

[29] Hoek, E. and Brown, E.T. Underground Excavations in Rock. London Institution of Mining and Metallurgy, London, 1980, 527 p.

[30] Deng, J. J. borehole stability prediction technology. Petroleum Industry Press, 2008.

[31] Liu, Y. Y., Pan, M., & Liu, S. Q. Petrel2ANSYS: Accessible software for simulation of crustal stress fields using constraints provided by multiple 3D models employing different types of grids. Journal of Central South University, 2019, 26(9), 2447-2463.

[32] Hashimoto, C., & Matsu'Ura, M. 3-D Simulation of Tectonic Loading at Convergent Plate Boundary Zones: Internal Stress Fields in Northeast Japan. Pure & Applied Geophysics, 2006, 163(9), 1803-1817.

[33] Zeng, W., Ding, W., Zhang, J., Zhang, Y., Guo, L., Kai, J. Fracture development in Paleozoic shale of Chongqing area (south China). Part two: numerical simulation of tectonic stress field and prediction of fractures distribution. Asian Earth Sci. 2013, 75 (8), 267–279.

[34] Jiu, K., Ding, W., Huang, W., You, S., Zhang, Y., Zeng, W. Simulation of paleotectonic stress fields within Paleogene shale reservoirs and prediction of favorable zones for fracture development within the Zhanhua Depression, Bohai Bay Basin, east China. Pet. Sci. Eng. 2013, 110, 119–131.

[35] Guo, P., Yao, L., Ren, D. Simulation of three-dimensional tectonic stress fields and quantitative prediction of tectonic fracture within the Damintun Depression, Liaohe Basin, northeast China. Struct. Geol. 2016, 86, 211–223.

[36] Liu, J., Ding, W., Yang, H., Wang, R., Yin, S., Li, A., & Fu, F. 3D geomechanical modeling and numerical simulation of crustal stress fields in shale reservoirs: a case study of the lower Cambrian Niutitang formation in the Cen'gong block, South China. Tectonophysics, 2017, 712, 663-683.

[37] Liu, Y. Y., Pan, M., & Liu, S. Q. Petrel2ANSYS: accessible software for simulation of crustal stress fields using constraints provided by multiple 3D models employing different types of grids. Journal of Central South University, 2019, 26(9), 2447-2463.

[38] Xiang, C. G., Zhang, J.H., & Wang, J. C. Application of geomechanics in geology-engineering integration. China Petroleum Exploration, 2017, 22(1), 75-88.

[39] https://www.bakerhughes.com/products-and-services/reservoir-development-services/reservoir-software/rs-geomechanics/rs-jewelsuite-geomechanics.

[40] http://www.gridworld.com.cn/.

[41] Luo G.Q. Three-dimensional crustal stress Field Calculation Framework and Display Method Research. China University of Petroleum (Beijing). 2018.

[42] Darley, H.C.H. A laboratory investigation of borehole stability. Journal of petroleum technology, 1969, 21(7): 883-892.

[43] Yan J.N. Drilling fluid technology. University of Petroleum Press, 2001.

[44] Lei Y.C., Xiang X.J. Brief Introduction of the Classification of Shales. Drilling fluid and completion fluid. 2007, 02: 63-66.

[45] Wang P.Q. The Study for Quantitative Analysis of Water Absorbed on Clays and Their Hydration Mechanism:(PHD dissertation). Southwest Petroleum Institute, 2001.

[46] Choi S, Crosson G, Mueller K T, et al. Clay mineral weathering and contaminant dynamics in a caustic aqueous system: II. Mineral transformation and microscale partitioning. Geochimica et Cosmochimica Acta. 2005, 69(18): 4437-4451.

[47] Curtis C D, Murchison D G, Berner R A, et al. Clay mineral precipitation and transformation during burial diagenesis [and discussion]. Philosophical Transactions of the Royal Society of London. Series A, Mathematical and Physical Sciences. 1985, 315(1531): 91-105.

[48] Środoń, J., Drits, V. A., McCarty, D. K., Hsieh, J. C., & Eberl, D. D. Quantitative X-ray diffraction analysis of clay-bearing rocks from random preparations. Clays and Clay Minerals, 2001, 49(6), 514-528.

[49] Deng H. Study on hydration stability of fractured shale and its application:(PHD dissertation). Southwest Petroleum Institute, 2004.

[50] Yu B.H. Study on mechanical mechanism of borehole instability in stratified shale formation. Beijing: (PhD Dissertation). China University of Petroleum (Beijing), 2006.

[51] Shen M.R., Chen J.F. Rock Mechanics. Shanghai: Tongji University Press, 2006, 7.

[52] Heard, H.C. Steady-state flow in polycrystaline halite at Pressure of 2Kpa, flow and fracture of rocks. Geophysical Monograph, 1963, No.16: 191-209.

[53] Oliver, M. A., & Webster, R. Kriging: a method of interpolation for geographical information systems. International Journal of Geographical Information System, 1990, 4(3), 313-332.

[54] Liu, J. , Ding, W. , Yang, H. , Wang, R. , Yin, S. , & Li, A. , et al. 3d geomechanical modeling and numerical simulation of crustal stress fields in shale reservoirs: a case study of the lower cambrian niutitang formation in the cen'gong block, south china. Tectonophysics, 2017, 712–713, 663-683.

[55] Yin, S., Ding, W., Zhou, W., Shan, Y., Xie, R., Guo, C., ... & Wang, X. crustal stress field evaluation of deep marine tight sandstone oil reservoir: A case study of Silurian strata in northern Tazhong area, Tarim Basin, NW China. Marine and Petroleum Geology, 2017, 80, 49-69.

[56] A, A. M. L., & B, N. S. M. Improved pseudo three-dimensional model for hydraulic fractures under stress contrast. International Journal of Rock Mechanics and Mining Sciences, 2020, 130.

[57] Wang H.C., Zhao W.H., & Guo B.B. Mohr-Coulom by Yield Criterion in Rock Plastic Mechanics. Chinese Journal of geophysics, 2012, 55(12), 4231-4238.

[58] Chen M.，Jin Y.，Zhang G.Q. Petroleum engineering related rock mechanics. Beijing：Science Press，2008：299-305.